Glial Reactivity and Cognitive Decline Follow Chronic Heterochromatin Loss in Neurons

Authors: A.G. Newman[1*], J. Sharif[2], P. Bessa[1], S. Zaqout[1,3], J. Brown[1§], D. Richter[1], R. Dannenberg[1], M., Nakayama[4], S. Mueller[5,6], T. Schaub[1], S. Manickaraj[1], P. Böhm-Sturm[5,6], O. Ohara[4,7], H. Koseki[2], P.B. Singh[1,8,#,*], V. Tarabykin[1,#,*]

Affiliations:

[1]Institute of Cell and Neurobiology, Charité – Universitätsmedizin Berlin, Corporate member of Freie Universität Berlin, Humboldt-Universität zu Berlin and Berlin Institute of Health (BIH), Berlin, Germany

[2]Developmental Genetics Laboratory, Center for Integrative Medical Sciences (IMS), RIKEN National Research and Development Agency, 1-7-22 Suehiuro-cho, Tsurumi-ku, Yokohama-shi, Kanagawa-ken, Japan 230-0045

[3]Department of Basic Medical Sciences, College of Medicine, QU Health, Qatar University, Doha, Qatar

[4]Laboratory of Medical Omics Research, Department of Frontier Research and Development,
Kazusa DNA Research Institute, 2-6-7 Kazusa-Kamatari, Kisarazu, Chiba 292-0818, Japan

[5]Department of Experimental Neurology and Center for Stroke Research, Charité – Universitätsmedizin Berlin, corporate member of Freie Universität Berlin, Humboldt-Universität zu Berlin and Berlin Institute of Health (BIH), Berlin, Germany

[6]NeuroCure Cluster of Excellence and Charité Core Facility 7T Experimental MRIs, Charité – Universitätsmedizin Berlin, Berlin, Germany

[7]Laboratory for Integrative Genomics, RIKEN Center for Integrative Medical Sciences, 1-7-22 Suehiro-cho, Tsurumi, Yokohama, Kanagawa 230-0045, Japan

[8]Department of Medicine, Nazarbayev University School of Medicine, 5/1 Kerei, Zhanibek Khandar Street, Nur-Sultan Z05K4F4, Kazakhstan

#These Authors Jointly supervised this work

*For Correspondence: andrew.newman@charite.de (A.G.N); prim.singh@nu.edu.kz (P.B.S.); victor.tarabykin@charite.de (V.T).

[§]Present Address: Department of Immunology and Inflammation Imperial College London, Commonwealth Building, The Hammersmith Hospital, Du Cane Road, London W12 0NN

Abstract

In aging cells and animal models of premature aging, heterochromatin loss coincides with transcriptional disruption including the activation of normally silenced endogenous retroviruses (ERVs). Here we show that loss of heterochromatin maintenance and de-repression of ERVs results in a chronic inflammatory environment characterized by neurodegeneration and cognitive decline. We discovered differential contributions of HP1 proteins to ERV silencing where HP1γ is necessary and sufficient for H4K20me3 deposition and HP1β deficiency causes aberrant DNA methylation. Combined loss of HP1β and HP1γ resulted in loss of DNA methylation at ERVK elements. Progressive ERV de-repression in HP1β/γ DKO mice was followed by stimulation of the integrated stress response, an increase of Complement 3+ reactive astrocytes and phagocytic microglia. This chronic inflammatory state coincided with age-dependent reductions in dendrite complexity and cognition. Our results demonstrate the importance of preventing loss of epigenetic maintenance, as this will be the only way postmitotic neuronal genomes can be protected and/or renewed.

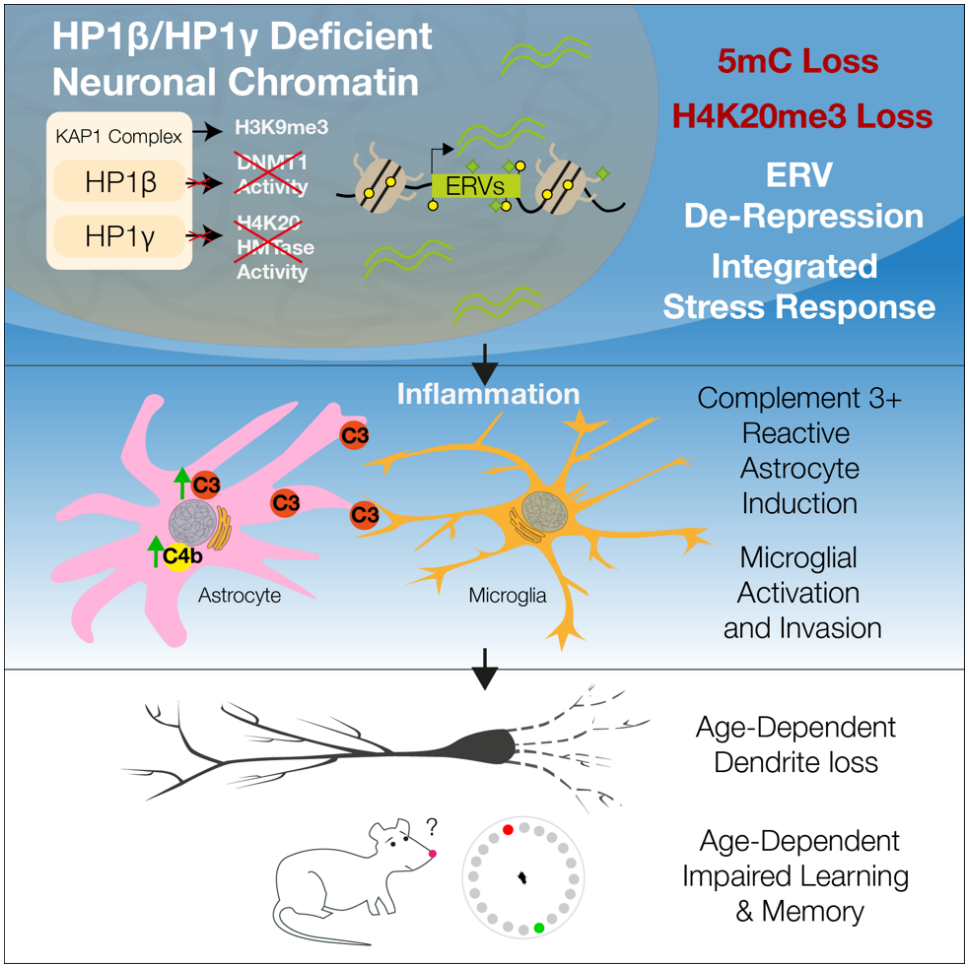

Introduction

Aging neurons operate under conditions of high cellular stress without renewal by cell division. Under normal physiological conditions, neurons continuously break their own DNA at enhancer regions [1,2], and their high metabolic rate results in an excess of reactive oxygen species harmful to protein and DNA integrity[3]. Neuronal genes most sensitive to oxidative DNA damage are downregulated with age[4], resulting in either cell death or cascading dysfunction and de-differentiation[5].

Little is known about what occurs in heterochromatin in aging neurons. However, in other cell types and human progeria models, a loss of DNA methylation[6,7], histone 3 lysine 9 tri-methylation (H3K9me3) and associated proteins is observed with age[8-10], along with a decreased association of heterochromatin with the nuclear lamina[11]. These age-related changes result in the activation of normally silenced repetitive elements such as endogenous retroviruses (ERVs)[12]

77 and Long Interspersed Nuclear Elements (LINEs)[10]. Elevated transcription of ERVs
78 have been observed in pathological states such as exogenous viral infections[13,14],
79 cancer[15], neurodegeneration[16,17], multiple sclerosis[18,19], ALS[20], and Alzheimer's
80 disease[17]. Elevated levels of ERVs have also been seen in models examining factors
81 associated with neurodegenerative diseases such and Tau[21] and TDP-43[22], while α-
82 synuclein has been shown to affect chromatin and the maintenance of ERVs
83 directly[23,24]. However, a causal relationship between ERVs and the initiation of
84 neurodegeneration has yet to be determined.

85 ERVs are silenced by the KAP1 repressor complex which recruits histone de-
86 acetylases, DNA methyltransferases, and histone methyltransferases and several
87 cofactors to induce heterochromatin formation (reviewed in [25]). Here, the histone
88 methyltransferase SETDB1 catalyzes H3K9me3 methylation[26], which serves as a
89 high-affinity binding site for Heterochromatin Protein 1 (HP1)[27,28], which facilitates
90 compaction and silencing[29].

91 We mimicked age-related heterochromatin loss by deletions of members of
92 the HP1 family in the mouse brain. Unlike other mutants of enzymatic epigenetic
93 modifiers—which typically have severe developmental phenotypes—the removal of
94 HP1 proteins mimics the destabilization normally seen in aged cells, whose lower
95 levels of H3K9me3 naturally result in less HP1 binding, activity, and stability. In
96 doing so, we describe the molecular contributions of HP1β (*Cbx1*) and HP1γ (*Cbx3*)
97 to ERV silencing and uncover an endogenous cause of the known age-related
98 increases[30,31] of Complement in the brain.

99 All three HP1 homologs are robustly expressed in post-mitotic neurons (fig
100 S1a,b). To test whether heterochromatin loss can drive neuronal aging *in vivo*, we
101 engineered mice to be conditionally deficient for HP1β and HP1γ in the cerebral
102 cortex using the *Emx1*^{Cre} deleter mouse strain. We observed a partial malformation
103 of the infrapyramidal blade of the dentate gyrus (DG) due to depletion of Ki67+

104 progenitors following loss of HP1β (fig **S1c,d**), which is consistent with HP1β's
105 established role in mitotic stability[32]. Apart from this minor developmental defect,
106 we detected no overt changes in cortical cytoarchitecture in HP1 single and double
107 mutants (fig. **S1e,f**), making these mutants a suitable model to study the long-term
108 effects of HP1-related heterochromatin loss.

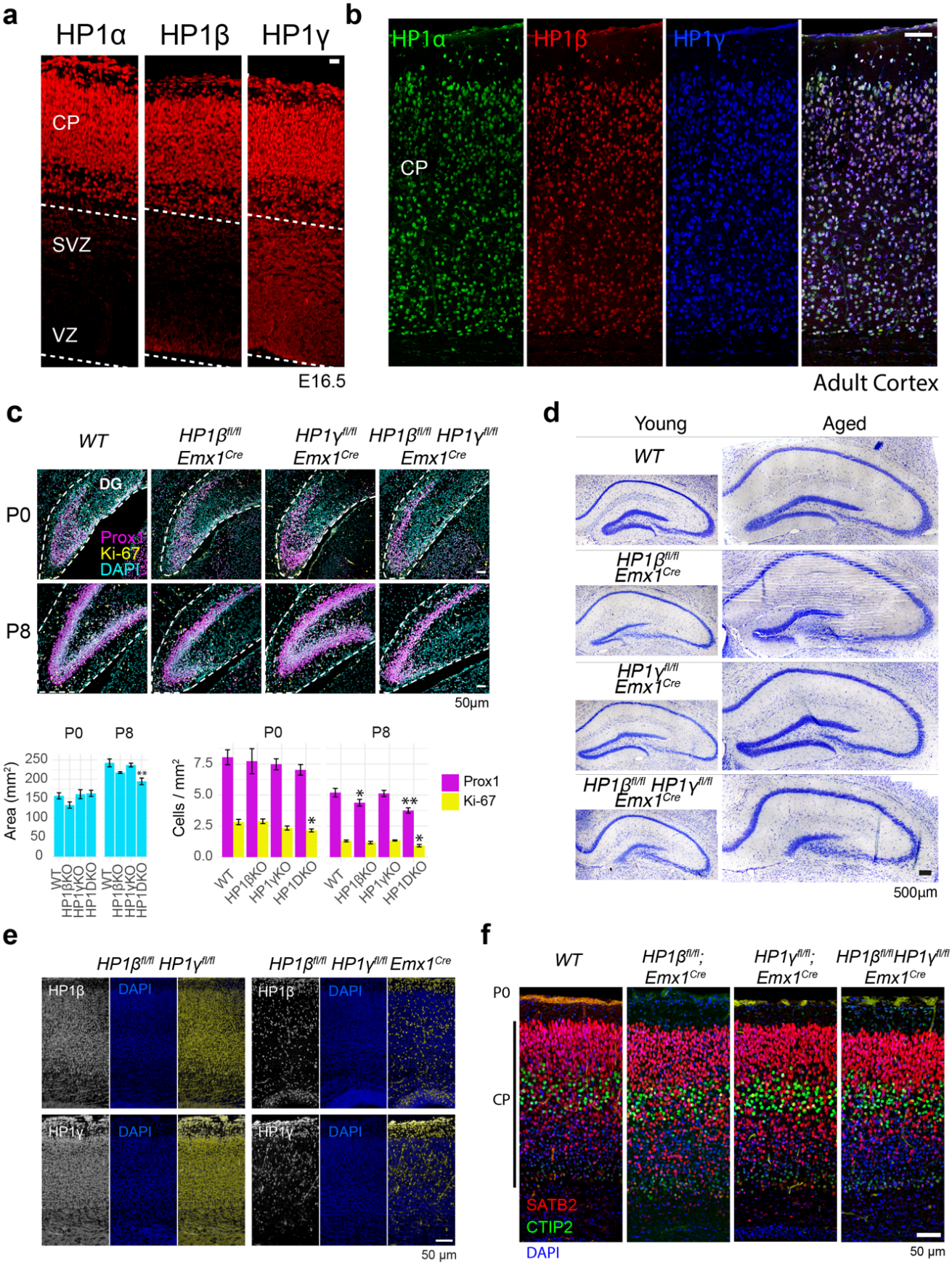
a
HP1α
HP1β
HP1γ
CP
SVZ
VZ
E16.5
b
HP1α
HP1β
HP1γ
CP
Adult Cortex
c
WT
HP1β fl/fl Emx1 Cre
HP1γ fl/fl Emx1 Cre
HP1β fl/fl HP1γ fl/fl Emx1 Cre
P0
P8
DG
Prox1
Ki-67
DAPI
50µm
Area (mm²)
Cells / mm²
Prox1
Ki-67
WT
HP1βKO
HP1γKO
HP1DKO
d
Young
Aged
WT
HP1β fl/fl Emx1 Cre
HP1γ fl/fl Emx1 Cre
HP1β fl/fl HP1γ fl/fl Emx1 Cre
500µm
e
HP1β fl/fl HP1γ fl/fl
HP1β fl/fl HP1γ fl/fl Emx1 Cre
HP1β
HP1γ
DAPI
50 µm
f
WT
HP1β fl/fl; Emx1 Cre
HP1γ fl/fl; Emx1 Cre
HP1β fl/fl HP1γ fl/fl Emx1 Cre
P0
CP
SATB2
CTIP2
DAPI
50 µm

110 **Figure S1 (previous page).** Expression of HP1 proteins and deletion from the
111 cerebral cortex. **a** HP1α and HP1β expression is strongest in post-mitotic neurons
112 of the cortical plate (CP) at embryonic day 16.5. Both are also expressed in
113 progenitor cells in the Subventricular and ventricular zones (SVZ and VZ,
114 respectively). HP1γ expression is much more uniformly expressed across
115 progenitor and post-mitotic cell types. (scale bar = 50 μm) **b** HP1 proteins remain
116 robustly expressed in the cortical plate of adult mice (scale bar = 100μm). **c**
117 Dentate gyri of HP1βKO and HP1β/γKO animals show malformation of the
118 infrapyramidal blade due to mitotic exhaustion between postnatal day 0 and
119 postnatal day 8. P0 WT n = 10, P0 HP1βKO n = 4, P0 HP1γKO n = 7, P0 HP1DKO
120 n= 11, P8 WT n = 4, P8 HP1βKO n = 3, P8 HP1γKO n = 4, P8 HP1DKO n= 5. One
121 way ANOVA with Dunnett's Multiple Comparison test where ** denotes $p < 0.05$,
122 and * denotes $p < 0.01$. **d** The morphology of young (3 month) and aged (13
123 month) hippocampi. **e** Emx1-Cre mediated deletion of floxed HP1 proteins results
124 in targeted deletion of HP1β and HP1γ in the pyramidal lineage seen here at
125 postnatal day 0 (P0). **f** Single or double deletion of HP1β or HP1γ does not
126 adversely affect neuronal cell fate or laminal position in the cerebral cortex at P0.

127

128

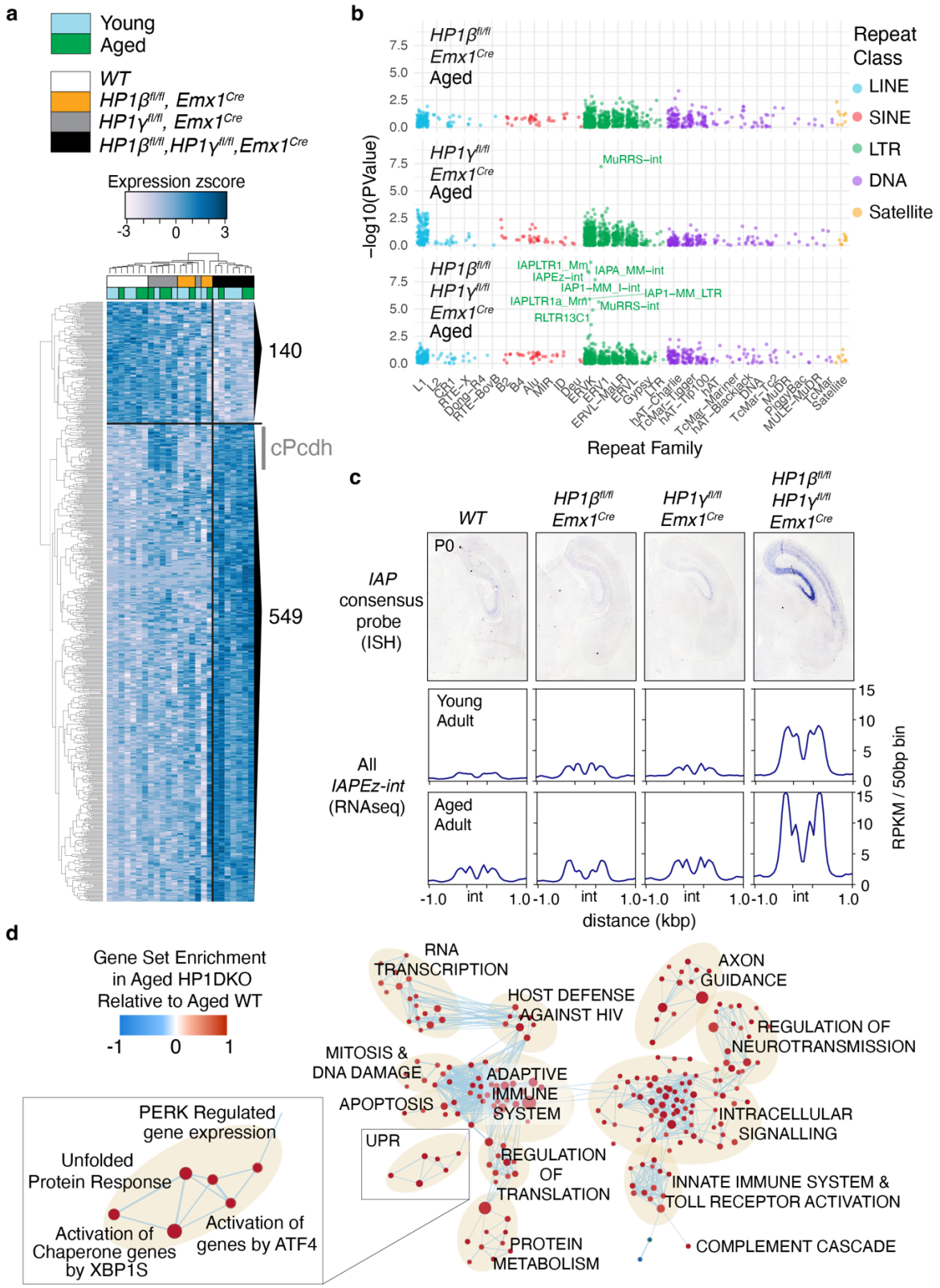

Figure 1. Loss of both HP1β and HP1γ results in activation of noncoding elements and induction of the integrated stress response. **a** Genes (inc. repetitive elements) significantly changed in young and aged *HP1β*$^{fl/fl}$*HP1γ*$^{fl/fl}$*Emx1*^{Cre} hippocampi (689 genes, corrected p <0.05). **b** Pseudo-Manhattan plot of significant changes to repetitive element transcription in aged HP1 mutants. Repeats from the ERVK

subfamily, which contains the evolutionarily recent *IAP*s, is most strongly affected in *HP1β*$^{fl/fl}$*HP1γ*$^{fl/fl}$*Emx1*^{Cre} hippocampi. **c** *In situ hybridization* using a consensus probe for IAP in P0 brains and RNAseq read coverage over the IAPEz internal fragment in young and aged adults (read coverage is RPKM normalized reads per 50bp bin). Gene Set Enrichment of upregulated transcripts **d** shows several affected pathways including host defense, Toll Receptor activation, unfolded protein response and the complement cascade.

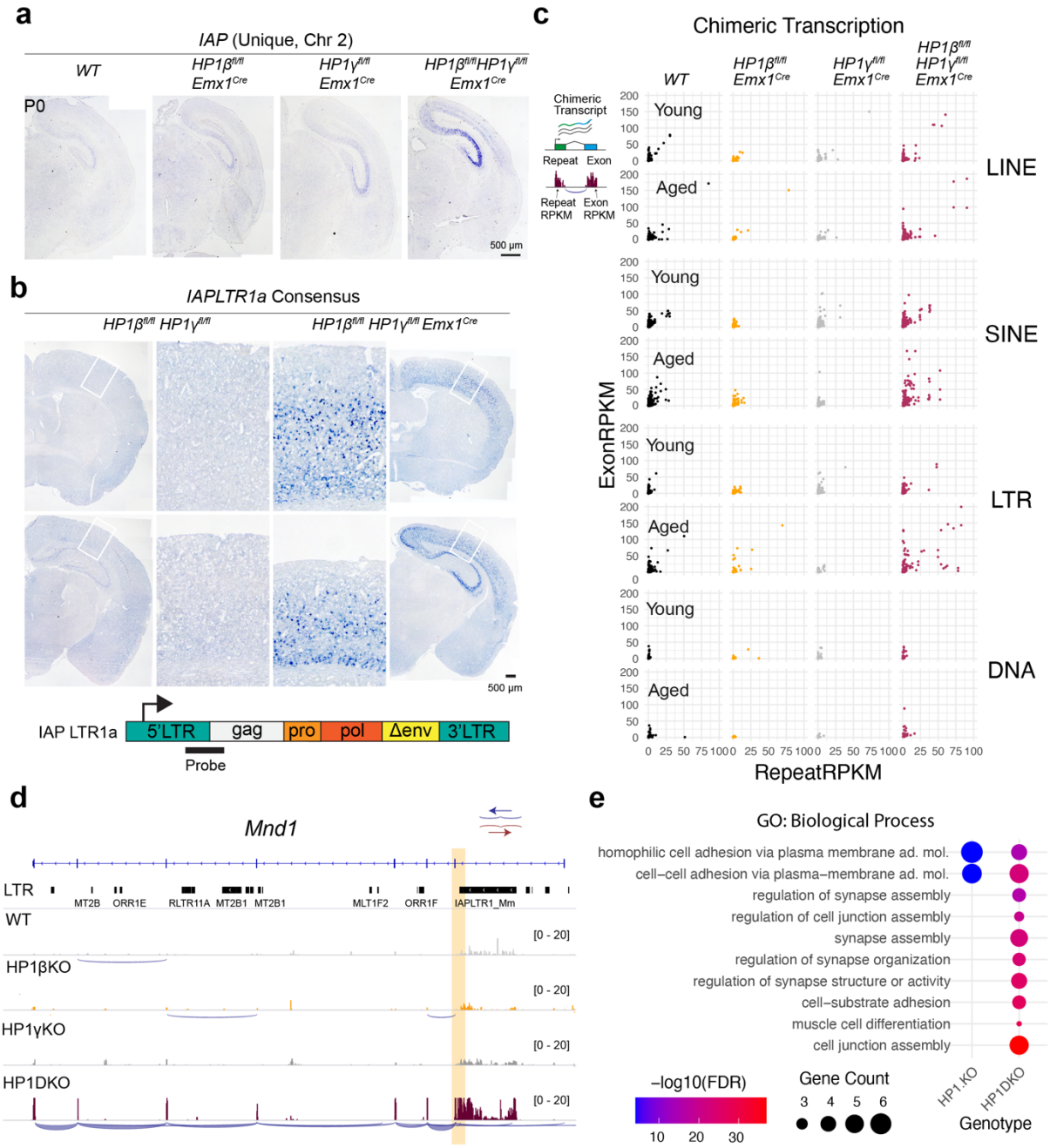

Figure S2. Sustained de-repression of ERVs and induction of chimeric transcripts in HP1DKO mutants. **a** In situ hybridization on P0 brains using an RNA probe specific for a single IAP element on chromosome 2. **b** In situ hybridization on

146 adult brains using an RNA probe that recognizes an IAPLTR1a consensus
147 sequence found on at least 196 IAPs. **c** Co-transcription plots of chimeric
148 transcripts where each point represents a chimeric transcript. **d** An example
149 chimeric transcript; transcriptional activation of an IAP element in the first intron of
150 *Mnd1* results in transcriptional activation of the entire gene. Shown here are
151 RNAseq tracks from aged genotypes. **e** Gene Ontology of significantly changed
152 genes (edgeR FDR <0.05) in *HP1β*$^{fl/fl}$*Emx1*^{Cre}, *HP1γ*$^{fl/fl}$ *Emx1*^{Cre}, and *HP1β*$^{fl/fl}$ *HP1γ*$^{fl/fl}$
153 *Emx1*^{Cre} RNAseq. No significant gene ontology could be observed for
154 *HP1β*$^{fl/fl}$*Emx1*^{Cre}. The differential expression of protocaherins in *HP1γ*$^{fl/fl}$ *Emx1*^{Cre},
155 and *HP1β*$^{fl/fl}$ *HP1γ*$^{fl/fl}$ greatly biases gene ontology towards cell adhesion and
156 synapse gene sets.

157

158 **Results**

159 **HP1 deficiency results in de-repression of ERVs and an innate immune**
160 **response**

161 Given the known role of HP1 proteins in maintaining repression of non-
162 coding elements [33], we performed cRNA-RNA *in situ* hybridization for the murine
163 endogenous retrovirus (ERV) Intracisternal Alpha Particle (IAP) and could observe
164 its robust de-repression in the HP1β/γ DKO, which was especially strong in the
165 hippocampus and absent from the dentate gyrus (fig. **1** & **S2b**). RNAseq on young
166 and aged hippocampi (fig. 1a) confirmed that repeats and chimeric transcripts were
167 de-repressed in HP1β/γ DKO (fig. **1b,c**, **S2c,d** & Data S1). The same analysis
168 revealed that apart from repeats and chimeric transcripts, the primary sources of
169 genotype-dependent variance fell into three further categories (fig. **1a**, Data S1):
170 The first are dentate gyrus related genes underrepresented in HP1βKO and HP1β/γ
171 DKO (140) such as Prox1, Dsp, Trpc6, Plk5 and Cdh9 (Data S1). The remaining two
172 categories were upregulated (549): first, expression of the entire protocadherin
173 cluster (cPcdh) was elevated in HP1γKO and HP1β/γ DKO (which is further observed
174 in gene ontology analyses (fig. **S2e**)), as were a small subset of canonical and non-
175 canonical imprinted genes (Data S1). Second, in HP1β/γ DKO we observed changes

176 in genes related to inflammation including innate immune pathways and unfolded
177 protein response (UPR) (fig. **1b**).

178

179 **HP1γ is required for H4K20me3 deposition and regulation of Protocadherin**
180 **genes**

181 To understand the epigenetic pathway by which HP1β and HP1γ regulate
182 repression of ERVs, we investigated the effect of HP1β and HP1γ mutations on the
183 HP1-related histone modifications H3K9me3 (histone 3 lysine 9 trimethylation) and
184 H4K20me3 (histone 4 lysine 20 trimethylation). H3K9me3-bound HP1 can recruit
185 Suv420h1/2 HMTases and direct local H4K20me3 deposition[34], and both histone
186 modifications are abundant in wt post-mitotic neurons (fig. **2a, S3a**). We found that
187 H3K9me3 remained unchanged (fig. **2a**) but observed a specific loss of H4K20me3
188 in specifically HP1γ-deficient neurons(fig. **2a, S3b**), consistent with previous
189 observations in spermatocytes[35]. We also found that HP1γ was sufficient for
190 H4K20me3 deposition because re-addition of HP1γ to HP1β/γ DKO cortices by *in*
191 *utero* electroporation at E14 restored H4K20me3, albeit not to the levels seen in
192 adjacent interneurons where HP1γ is not deleted (fig. **2b**). The H3K9me3-HP1γ-
193 H4K20me3 pathway also appears to regulate isoform selection at the protocadherin
194 (cPcdh) cluster. While all protocadherin isoforms can be observed in bulk RNAseq,
195 single neurons express a unique combination of protocadherin isoforms which is
196 clonally defined during neurogenesis[36–38]. Thus, bulk ChIPseq shows the
197 protocadherin cluster is marked with H3K9me3 and H4K20me3 (fig. **S3c**)
198 corresponding to single cell silencing of unused exons observed at the population
199 level. In the HP1γKO, H4K20me3 is lost and there is elevated expression of cPcdh
200 genes (fig. **1a**, **S3c**). Given the known requirement of the HP1 chromoshadow
201 domain (CSD) for association with the H4K20me3 HMTase Suv420h2[39], we carried
202 out co-immunoprecipitation and co-localization analysis to identify residues in the

203 CSD essential for the interaction of HP1γ with Suv420h2 (fig. **2c-e, S4**). Given that
204 the cPcdh cluster is regulated by the SETDB1 HMTase that generates H3K9me3[40],
205 it seems likely that a H3K9me3-HP1γ-H4K20me3 pathway might be an important
206 mechanism for regulating chromosomal domains, such as the protocadherin cluster
207 and clustered retrotransposons.

208

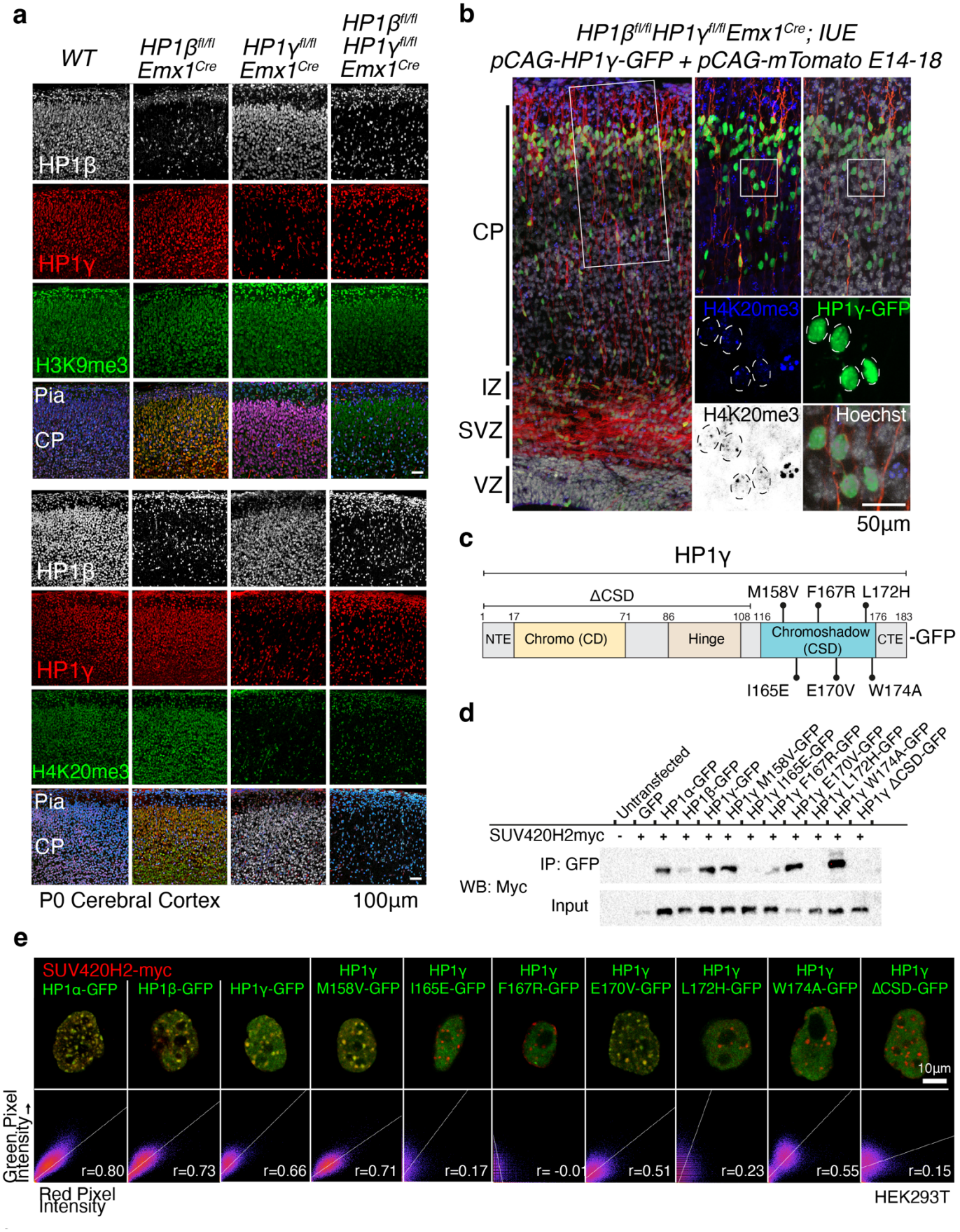
a
WT
HP1β fl/fl Emx1 Cre
HP1γ fl/fl Emx1 Cre
HP1β fl/fl HP1γ fl/fl Emx1 Cre
HP1β
HP1γ
H3K9me3
Pia
CP
H4K20me3
P0 Cerebral Cortex
100μm
b
HP1β fl/fl HP1γ fl/fl Emx1 Cre; IUE
pCAG-HP1γ-GFP + pCAG-mTomato E14-18
CP
IZ
SVZ
VZ
H4K20me3
HP1γ-GFP
Hoechst
50μm
c
HP1γ
ΔCSD
M158V F167R L172H
1 17 71 86 108 116 176 183
NTE
Chromo (CD)
Hinge
Chromoshadow (CSD)
CTE
-GFP
I165E E170V W174A
d
Untransfected
GFP
HP1α-GFP
HP1β-GFP
HP1γ-GFP
HP1γ M158V-GFP
HP1γ I165E-GFP
HP1γ F167R-GFP
HP1γ E170V-GFP
HP1γ L172H-GFP
HP1γ W174A-GFP
HP1γ ΔCSD-GFP
SUV420H2myc
IP: GFP
WB: Myc
Input
e
SUV420H2-myc
HP1α-GFP
HP1β-GFP
HP1γ-GFP
HP1γ M158V-GFP
HP1γ I165E-GFP
HP1γ F167R-GFP
HP1γ E170V-GFP
HP1γ L172H-GFP
HP1γ W174A-GFP
HP1γ ΔCSD-GFP
10μm
Green Pixel Intensity
Red Pixel Intensity
r=0.80
r=0.73
r=0.66
r=0.71
r=0.17
r= -0.01
r=0.51
r=0.23
r=0.55
r=0.15
HEK293T

Figure 2. HP1γ is necessary and sufficient for deposition of H4K20me3. **a** H3K9me3 levels are unchanged in HP1β and HP1γ deficient neurons. H4K20me3, is unaffected in wild-type interneurons but lost completely in HP1γ-deficient pyramidal neurons. **b** Re-addition of HP1γ into developing mutant brains by *in utero electroporation* can restore H4K20me3 (magnification, nuclei outlined by dashed circles). (CP = cortical plate IZ = intermediate zone, SVZ = subventricular zone, VZ = ventricular zone). **c** Schematic of HP1γ protein product with domains and point mutations tested. **d** Co-immunoprecipitation of SUV420H2 with HP1 proteins and point mutants confirms residues in the chromoshadow domain (CSD) of HP1γ are essential for its binding with SUV420H2. **e** Co-localization of C terminal GFP-tagged HP1α, HP1β, HP1γ and HP1γ mutants with C terminal myc-tagged SUV420H2.

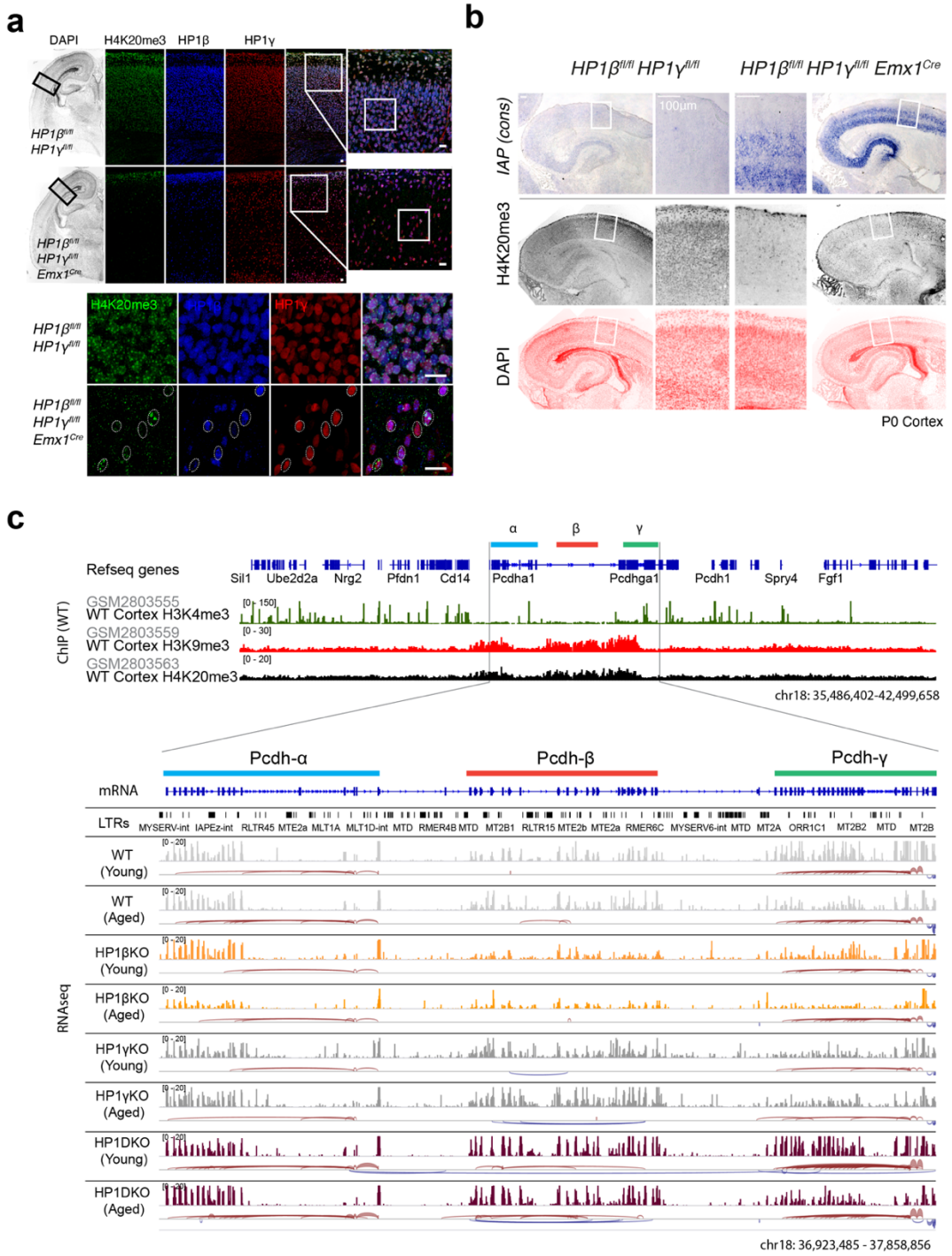

Figure S3. H4K20me3 loss is correlated with IAP de-repression and Protocadherin expression. **a** H4K20me3, normally abundant in post-mitotic cortical neurons is completely missing in HP1γ deficient Emx1-lineage pyramidal neurons. In cortices missing HP1γ, H4K20me3 can still be seen in adjacent wild type interneurons (see magnifications). All scalebars 50µm. **b** *In situ hybridization* of IAP consensus sequence alongside adjacent sections stained for H4K20me3 and Dapi. **c** HP1γ is required for transcriptional regulation of the protocadherin cluster. (Top): Reference gene annotation of the mouse protocadherin α β and γ clusters on

chromosome 18 along with published ChIPseq data of H3K4me3, H3K9me3 and H4K20me3 performed in cortical neurons [41]. (Bottom): mRNA and LTR reference annotation along with read coverage tracks from hippocampal RNAseq performed in this study.

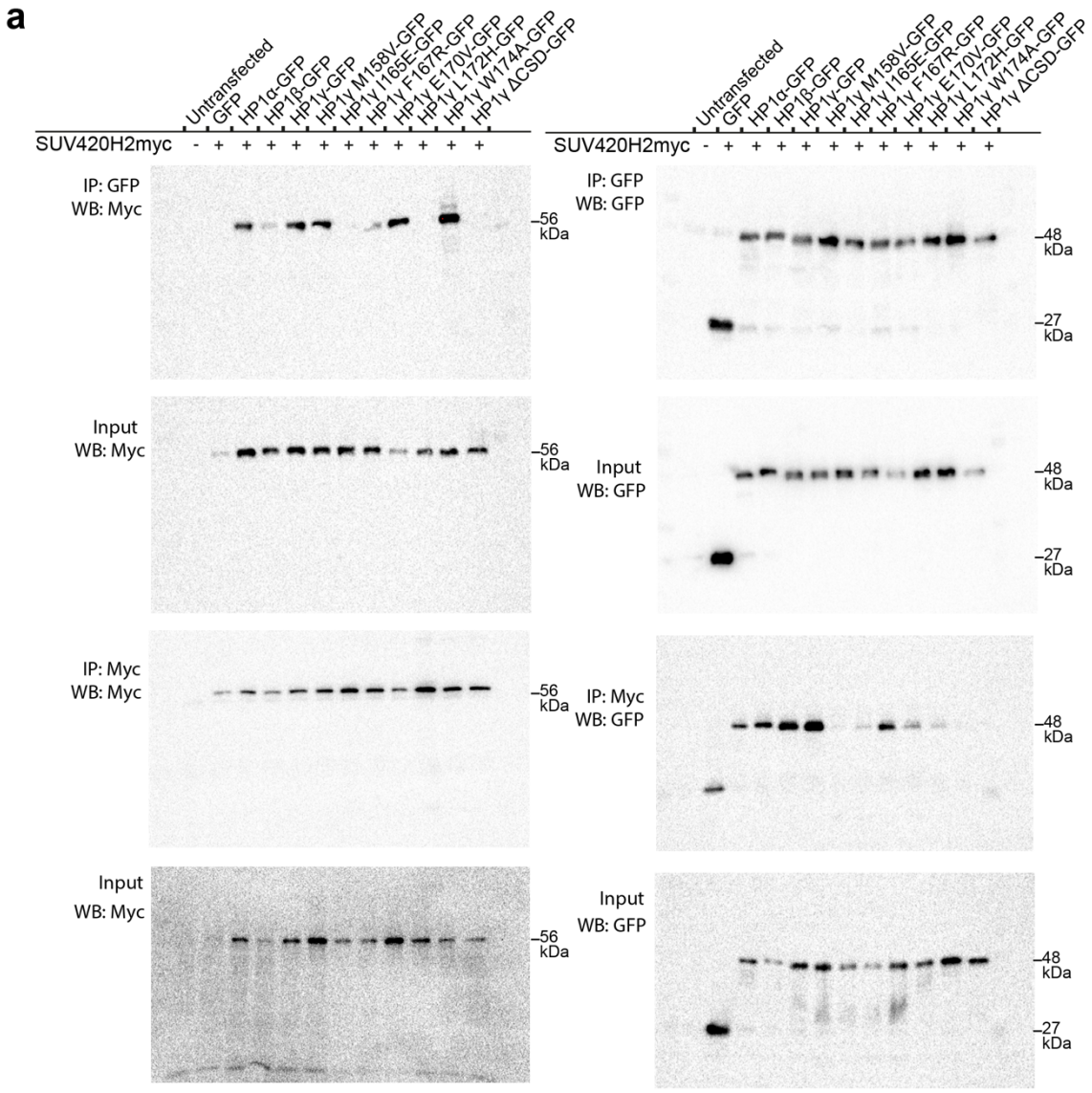

Fig. S4. (B) Full blots from Co-immunoprecipitation of SUV420H2myc with HP1-GFP proteins from Figure **2d**.

245 **HP1β deficiency results in aberrant DNA methylation**

246 Prominent increases in the expression of tissue specific imprinted genes
247 (Data S1) in HP1βKO and HP1β/γ DKO mutants indicated that DNA methylation may
248 be affected by HP1β deficiency.

249 We engineered an ES cell line that contains an ERT2-Cre transgene where all
250 three HP1 genes are floxed. This system allowed for the deletion of all three HP1
251 genes following the addition of tamoxifen, (thus termed HP1cTKO) that we then be
252 profiled for DNA methylation using reduced-read bisulfite sequencing (RRBS) and
253 changes to KAP1, H3K9me3 and H4K20me3 (Figure **3a**). We found that triple
254 deficiency of HP1 proteins results in reduced KAP1 at imprinting control regions
255 (ICRs) marked by ZFP57 (fig. **S5a**), while DNA methylation at these ICRs including
256 *Nnat* shows mixed changes (fig. **S5b,c**). KAP1 was unchanged over IAP elements in
257 HP1cTKO ES cells, with a reduction in H3K9me3 and an expected absence of
258 H4K20me3 (fig. **3b**). While ES cells are not expected to utilize protocadherins the
259 same way as neurons, regulatory H3K9me3 in the cPcdh is unaffected in HP1cTKO
260 ESCs despite H3K9me3 and H4K20me3 being lost at adjacent IAP elements (fig
261 **S5d**, arrows). This additionally suggests that regulatory H3K9me3 is unaffected in
262 *HP1γ$^{fl/fl}$ Emx1^{Cre}* mutants, and that it is disruption of the HP1γ-H4K20me3 pathway
263 that causes elevated Pcdh expression in *HP1γ$^{fl/fl}$ Emx1^{Cre}* and subsequently *HP1β$^{fl/fl}$*
264 *HP1γ$^{fl/fl}$ Emx1^{Cre}* brains.

265 DNA methylation can be used to accurately estimate the biological or
266 'epigenetic' age (eAge) of tissues, which increases at a steady rate in adult tissues [7].
267 While embryonic stem cells normally maintain an assigned eAge of zero [7], we were
268 surprised to find that the eAge of HP1cTKO ES cells increased faster than their time
269 in culture (fig. **3c**).

270

271

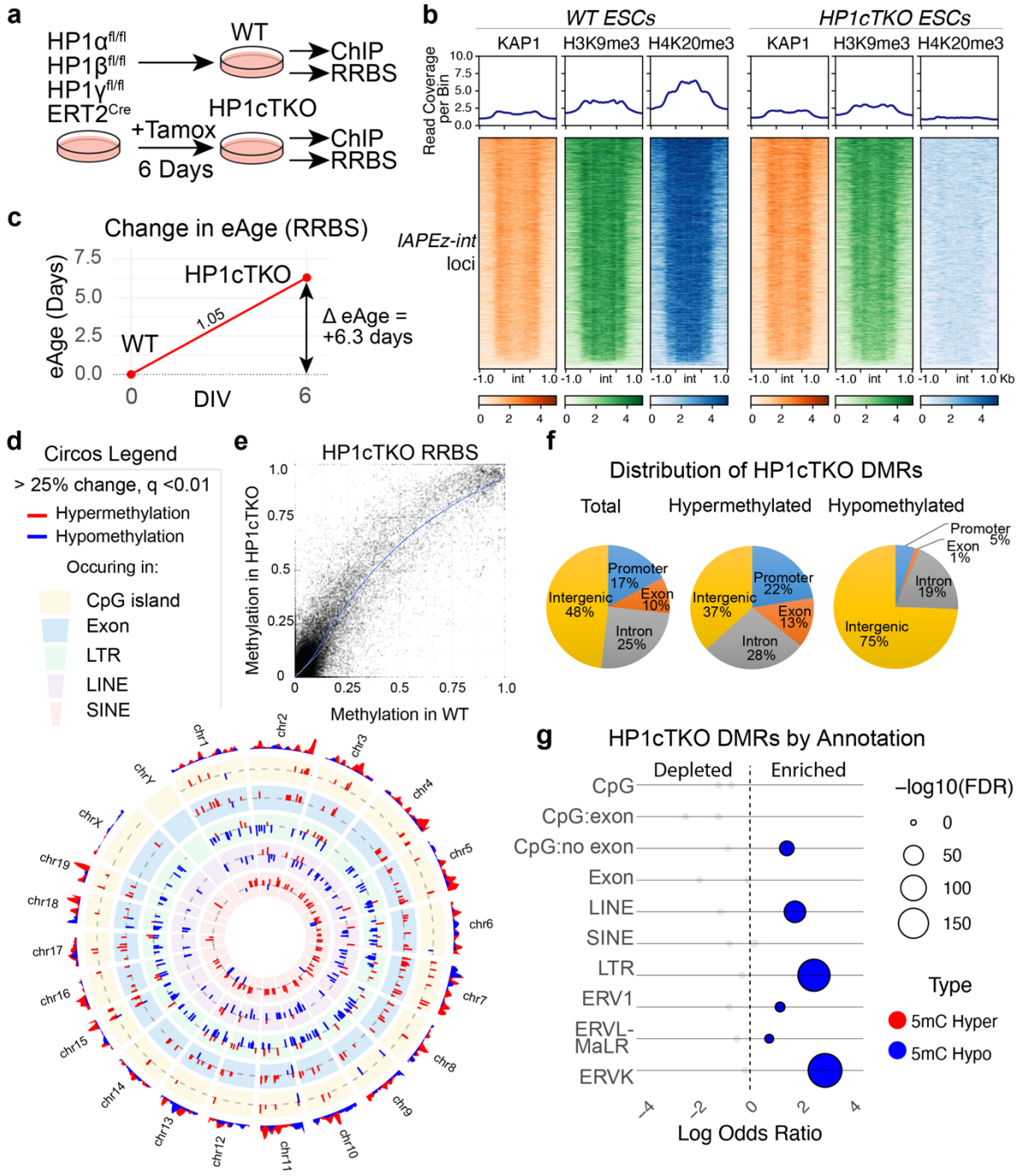

Figure 3 DNA methylation is further perturbed in HP1cTKO ES cells. **a** Schematic of the HP1cTKO RRBS experiment where *HP1a*$^{fl/fl}$*HP1β*$^{fl/fl}$*HP1γ*$^{fl/fl}$*ERT2*^{Cre} ES cells are left untreated (WT) or treated with tamoxifen (HP1cTKO) for 6 days in vitro before profiling DNA methylation status by Reduced Representation Bisulphite Sequencing (RRBS) and H3K9me3, H4K20me3 and KAP1 by ChIPseq. **b** Coverage of KAP1, H3K9me3 and H4K20me3 over *IAPEz internal segments (int)* and adjacent LTRs is reduced in HP1cTKO ES cells. Given the deletion of HP1γ in HP1cTKO, H4K20me3 is lost entirely. **c** Profiling of ~18,000 CpG sites in WT and HP1cTKO ES

282 cells reveals that deletion of HP1 proteins initiates a positive change in eAge. **d**
283 Circos plot of methylation changes that are greater than 25% ($q < 0.01$) plotted by
284 chromosome by annotation. The magnitude of change is represented on the radial
285 y axis. The outermost ring represents methylation change density. Inner rings
286 annotate methylation changes occurring to CpG islands, exons, LTRs, LINEs and
287 SINEs respectively. **e** Scatterplot of cytosine methylation observed in both HP1cTKO
288 and WT Reduced Representation Bisulfite Sequencing. **f** Distribution of HP1cTKO
289 Differentially Methylated Regions (DMRs) by genic feature. **g** HP1cTKO DMRs by
290 annotation, coloured if statistically significant by q value <0.01 and absolute
291 methylation difference is greater than 25%. (F) Odds ratios of overlap of significant
292 HP1cTKO DMRs plotted against the adjusted p value (FDR) of the respective
293 hypergeometric test.

294

295

296

297

298

299

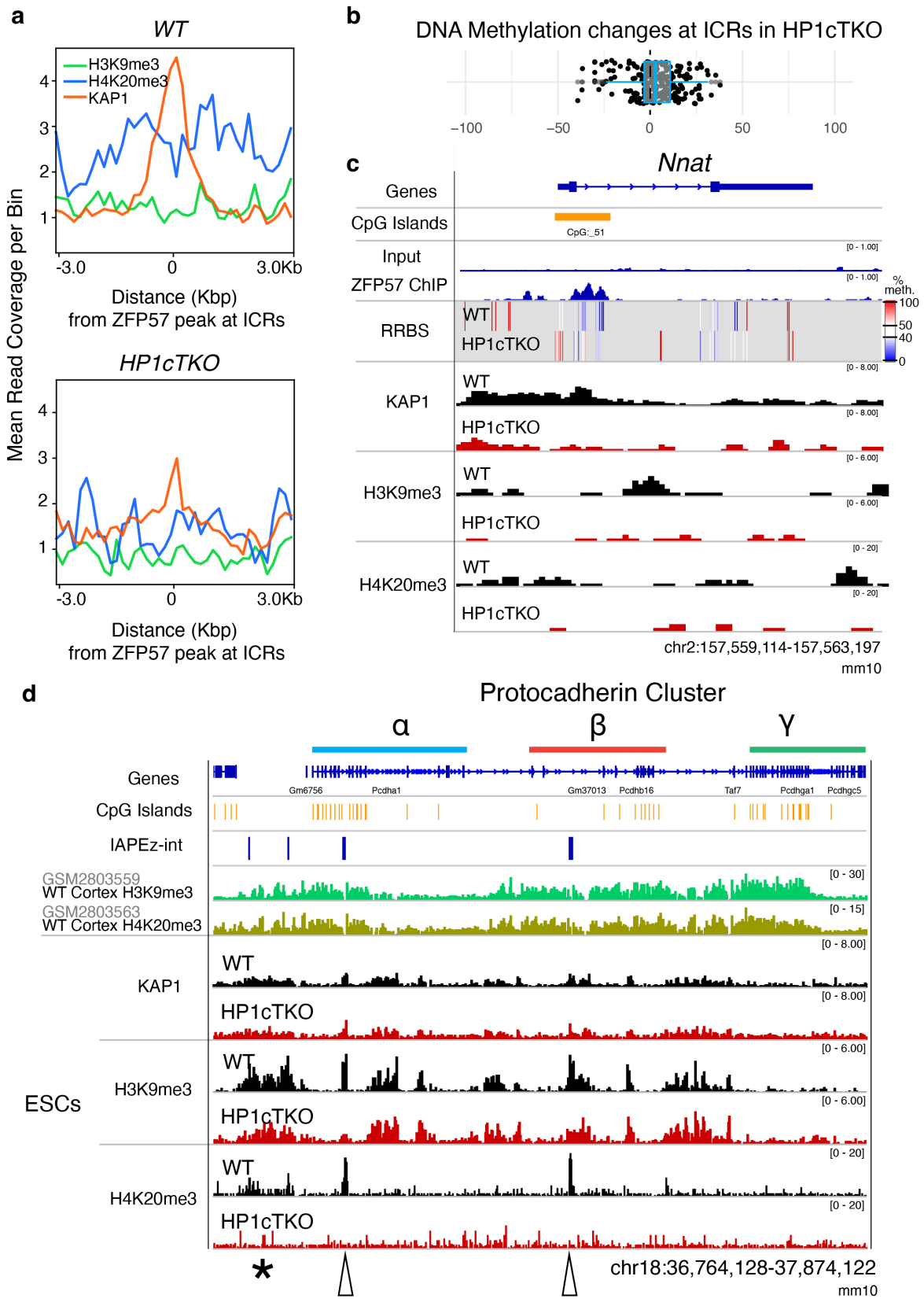

Figure S5. H3K9me3 is lost at repeats and ICRs but is unchanged at regulatory regions of the protocadherin cluster in HP1cTKO ES cells. **a** Read coverage of KAP1, H3K9me3 and H4K20me3 centred at ZFP57 peaks found at mouse imprinting control regions (ICRs) averaged over biological replicates. (RPGC-normalized

305 bigwigs were averaged, 50bp comatrices were used and profiles were plotted over
306 ICRs with a window of 150bp). **b** DNA Methylation changes at ICRs in HP1cTKO are
307 mixed but show a tendency towards 'hypermethylation' which would be consistent
308 with increased 5hmC observed in figure S5a. **c** Genome browser view of changes
309 occurring in HP1cTKO ESCs at imprinting control region found at Neuronatin (*Nnat*).
310 In addition to shifts in DNA methylation seen in the RRBS track, KAP1 is lost in
311 HP1cTKO ESCs surrounding the ICR (CpG island marked by ZFP57; ZFP57 ChIP
312 data from [42]). **d** Genome browser view of changes to KAP1, H3K9me3 and
313 H4K20me3 at the protocadherin locus in HP1cTKO ESCs with reference tracks for
314 refseq genes, CpGs, IAPEz-int, along with published ChIPseq of H3K9me3 and
315 H4K20me3 from the cortex [41]. H3K9me3 and H4K20me3 mark regulatory domains
316 over the protocadherin cluster in cortical neurons. At the same locus in embryonic
317 stem cells (ESCs), H3K9me3 can be seen at IAPs and regulatory domains, and in
318 HP1cTKO cells H3K9me3 is only lost at IAPs. H4K20me3 at the protocadherin
319 cluster in wt ES cells is prominently observed at IAP loci (empty arrows) and at the
320 proximal promoter (*), and is completely lost in HP1cTKO ESCs.
321
322

323 HP1cTKO ESCs displayed hypomethylation at LINEs and LTRs (particularly
324 ERVK) (fig. **3d,g**) despite a global shift towards hypermethylation (fig.**3e**) which is
325 also represented in promoters and gene bodies (fig **3f**). While a large number of
326 significantly hypermethylated cytosines overlap with CpGs, exons, SINEs (fig **3d**)
327 and ICRs (fig **S5b**), as annotation sets they do not show statistical significance based
328 on the hypergeometric test (Fig. 3g). This lack of significance may be attributed to
329 the global background shift towards hypermethylation.

330 Given that reduced representation bisulfite sequencing (RRBS) cannot
331 discriminate between 5-methyl cytosine (5mC) and 5-hydroxy-methyl cytosine
332 (5hmC), we surmised that some of the 'hypermethylation' observed in the HP1cTKO
333 RRBS samples may be attributable to active demethylation processes, specifically
334 the oxidation of 5mC to 5hmC mediated by TET enzymes.[43] We tested two specific
335 loci using primers designed to amplify over single HpaII/MspI (CCGG) sites from
336 hippocampal lysates. We found that cytosine methylation at Neuronatin (*Nnat)* is
337 decreased in an age-dependent manner in $HP1\beta^{fl/fl}$ $Emx1^{Cre}$ hippocampal lysates.
338 Similarly, $HP1\beta^{fl/fl}HP1\gamma^{fl/fl}Emx1^{Cre}$ hippocampal lysates showed age-dependent

339 decreases in 5mC methylation at IAP sequences alongside a trend towards
340 hydroxymethylation for both loci (fig. **S6a**).

341 To elucidate the full effects of HP1 deficiencies on 5mC and 5hmC, we
342 conducted RRBS both with and without prior oxidation on hippocampal lysates. This
343 oxidation step converts 5hmC into 5-formylcytosine (5fC), which does not undergo
344 bisulfite conversion, thereby allowing us to distinguish between 5mC and 5hmC (fig
345 **4a**). After an average 67% unique (+20% ambiguous) read mapping alignment
346 efficiency we found that bisulfite conversion using this method recovered on
347 average ~35% of Methylated CpGs (fig **4b**). This experiment yielded results largely
348 consistent with what was observed in HP1cTKO ESCs. We found that deficiency of
349 HP1β results in aberrant 5mC (*de novo*) hypermethylation of promoters and CpG
350 islands, a large percentage coming from a gene desert on chromosome 12 (**fig 4c-**
351 **e, S6c**). Surprisingly, we also found that clustered protocadherin promoters
352 became dramatically 5mC hypomethylated in HP1β/γ DKO hippocampi (fig **4e,**
353 **S6d**)., along with imprinting control regions (ZFP57 ICRs) (**fig 4e**). 5mC DNA
354 methylation at LTRs, primarily ERVK elements, was markedly reduced in
355 HP1β/γDKO hippocampi (**Figure 4e, S6e**). This effect is also likely an
356 underestimate given the lower mapability of repeats in RRBS sequencing and a
357 lower bisulfite conversion efficiency in this experiment. We could also observe
358 corresponding statistically significant increases in 5hmC over ERVK and IAPLTR1a
359 annotated regions in HP1β/γDKOs. Notably, single deficiency of either HP1β or
360 HP1γ already initiates drift in DNA methylation, evidenced by significant increases
361 in 5hmC over introns, LINEs, SINEs, and LTRs, an effect that is recapitulated in
362 normal aging in wildtype hippocampi (**fig. 4e**).

363

364

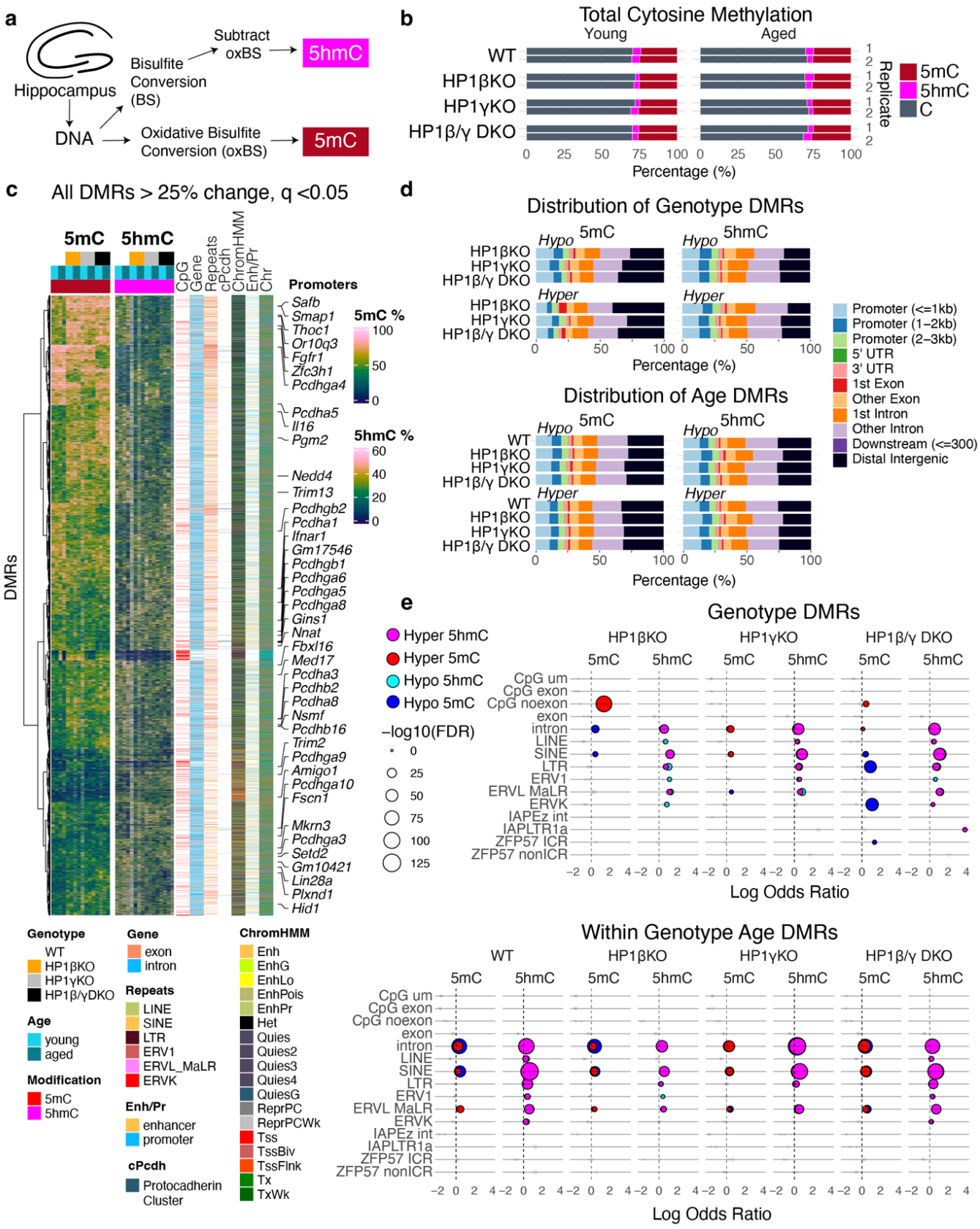

Figure 4. DNA methylation fidelity is progressively compromised in HP1 deficient hippocampi. **a** Schematic of experimental design showing determination of paired 5-methyl Cytosine (5mC) and 5-hydroxy-methyl Cytosine (5hmC) measurements

369 from young and aged *HP1β*$^{fl/fl}$;*Emx1*^{Cre}, *HP1γ*$^{fl/fl}$*Emx1*^{Cre} and *HP1β*$^{fl/fl}$*HP1γ*$^{fl/fl}$*Emx1*^{Cre}
370 mutant hippocampal lysates by Reduced Representation Bisulfite Sequencing
371 (RRBS). Genotypes that follow are abbreviated to HP1βKO, HP1γKO, and
372 HP1β/γDKO respectively for clarity. **b** Global 5mC and 5hmC methylation across
373 biological replicates sampled. **c** Heatmap of all observed Differentially Methylated
374 Regions (5mC or 5hmC) that change 25% or more and are statistically significant
375 below q = 0.05. DMRs (cytosine positions, rows) observed across genotypes are
376 accompanied by row annotations corresponding to genomic context denoted by
377 being a CpG island, in a gene (intron/exon), repetitive element (LINE, SINE, ERV1,
378 ERVL_MaLR, ERVK or other nonredundant LTRs), overlap with the protocadherin
379 cluster (denoted cPcdh), its chromatin state defined by the 18 state ChromHMM
380 model from P0 mouse cortex (ChromHMM), its overlap with promoters or
381 enhancers defined by the Enhancer-gene map from ENCODE 3, and chromosome
382 (Chr). **d** Total distribution of DMRs by genotype and direction of change
383 (hypomethylation 'hypo' or hypermethylation 'hyper'). **e** Odds Ratios of DMRs
384 significantly changed due to genotype or age are plotted against the q value (FDR)
385 resulting from the hypergeometric test of DMRs overlapping with the annotation.
386 CpG um = Unmasked CpGs, CpG exon = CpG islands overlapping with exons, CpG
387 noexon = CpG islands not overlapping with exons, LTR annotation here refers to all
388 LTRs including ERV1, ERVL MaLR, ERVK etc.

389

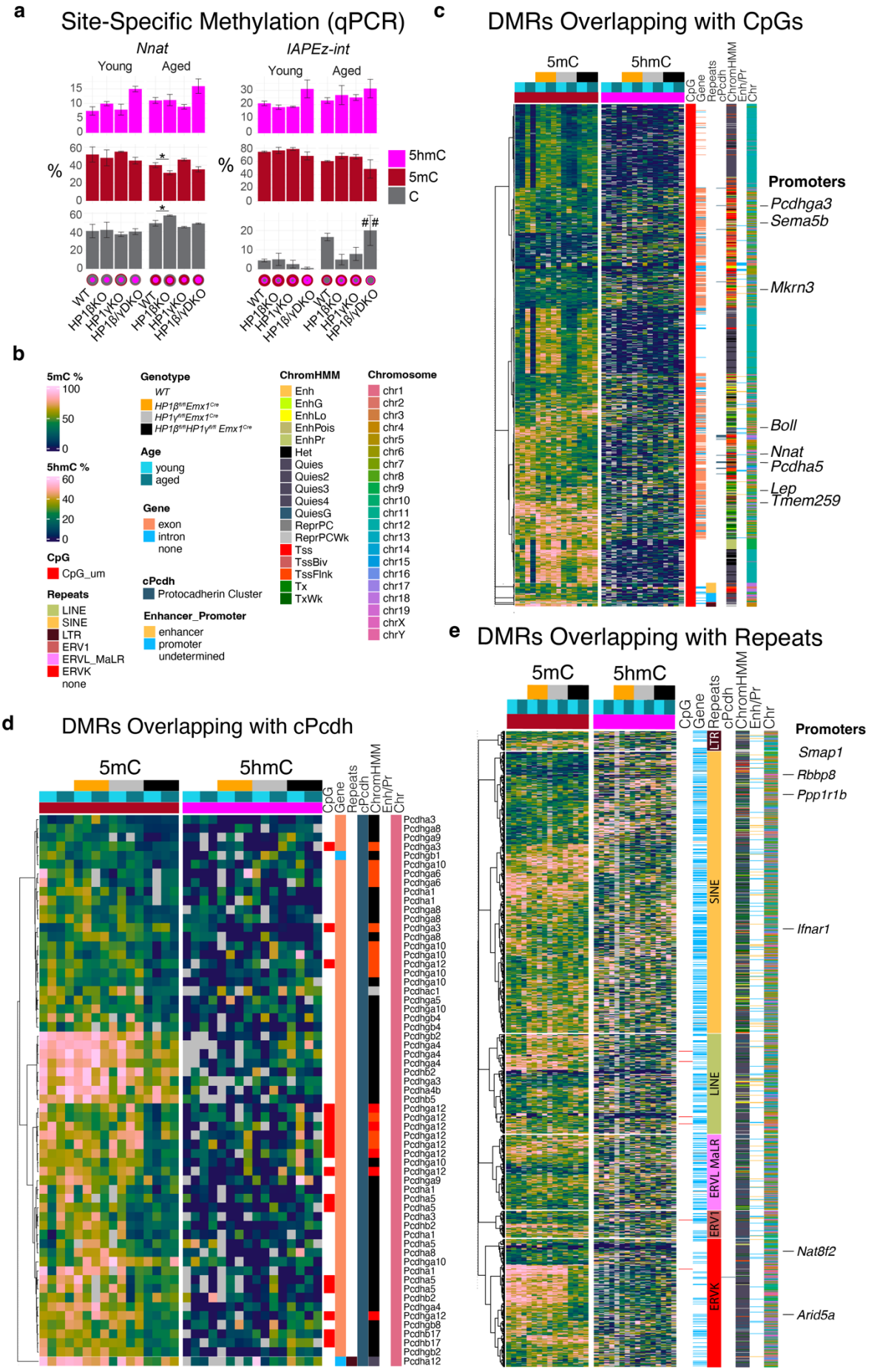
a
Site-Specific Methylation (qPCR)
Nnat
IAPEz-int
Young
Aged
%
5hmC
5mC
C
WT
HP1βKO
HP1γKO
HP1β/γDKO
b
5mC %
5hmC %
CpG
CpG_um
Repeats
LINE
SINE
LTR
ERV1
ERVL_MaLR
ERVK
none
Genotype
WT
HP1β^f/f Emx1^Cre
HP1γ^f/f Emx1^Cre
HP1β^f/f HP1γ^f/f Emx1^Cre
Age
young
aged
Gene
exon
intron
none
cPcdh
Protocadherin Cluster
Enhancer_Promoter
enhancer
promoter
undetermined
ChromHMM
Enh
EnhG
EnhLo
EnhPois
EnhPr
Het
Quies
Quies2
Quies3
Quies4
QuiesG
ReprPC
ReprPCWk
Tss
TssBiv
TssFlnk
Tx
TxWk
Chromosome
chr1
chr2
chr3
chr4
chr5
chr6
chr7
chr8
chr9
chr10
chr11
chr12
chr13
chr14
chr15
chr16
chr17
chr18
chr19
chrX
chrY
c
DMRs Overlapping with CpGs
5mC
5hmC
CpG
Gene
Repeats
cPcdh
ChromHMM
Enh/Pr
Chr
Promoters
Pcdhga3
Sema5b
Mkrn3
Boll
Nnat
Pcdha5
Lep
Tmem259
d
DMRs Overlapping with cPcdh
e
DMRs Overlapping with Repeats
Smap1
Rbbp8
Ppp1r1b
Ifnar1
Nat8f2
Arid5a
LTR
SINE
LINE
ERVL MaLR
ERV1
ERVK

391 **Figure S6.** DNA methylation is affected in several regions in HP1 deficient
392 hippocampi. **a** Profiles of qPCR-profiled cytosine hydroxymethylation (5hmC),
393 cytosine methylation (5mC) and unmethylated cytosines (C) at selected CCGG sites
394 in Neuronatin (*Nnat*) and IAPEz-int from hippocampal lysate DNA. Mean ±SEM; 3
395 biological replicates for each, two-way ANOVA, * = p <0.05 within age across
396 genotype, ## = p <0.01 within genotype across age. **b** Legend for heatmaps in **c,d,e**
397 for significant DMRs subset by row annotations corresponding to CpG islands, gene
398 body, repeats, P0 Cortex ChromHMM state and chromosome. **c** DMRs (% difference
399 > 25%, q < 0.05) overlapping annotated CpG islands. **d** DMRs (% difference > 25%
400 q < 0.05) occurring in the protocadherin cluster. **e** DMRs (% difference > 30%, q <
401 0.05) that overlap an annotated repeat.

402

403

404 **Activation of astrocytes and microglia**

405 We found that 15% of (88/565 protein coding) genes differentially expressed
406 in *HP1β*$^{fl/fl}$*HP1γ*$^{fl/fl}$*Emx1*^{Cre} hippocampi overlapped with cellular responses to
407 interferons including *Ifitm2*, *Ifi27* and the regulatory component of the interferon
408 gamma receptor *Ifngr2* (Data S1). HP1DKO hippocampi also showed increased
409 *Oas3*, *Lyk6*, *Wdfy4*, and *Il34*, but most notably displayed elevated transcription of
410 complement *C3, C4b* and *C1qa*.

411 Given the recently established importance of complement proteins in the
412 developing brain [44], their co-occurrence with amyloid plaques [45], and their
413 accumulation over normal aging [30,46], we performed a multiplex in situ hybridization
414 in order to identify the cell type(s) containing raised levels of Complement 3 (*C3*)
415 RNA (fig. **5a-i**). Elevated *C3* transcripts could be observed in the soma of wildtype
416 CA1 and CA3 neurons, but in aged HP1β/γ DKO, *C3* could also be detected in small
417 plaque-like foci in the *stratum radiatum* (white arrows, fig. **5d,g**) that were not
418 observed in any other condition. These foci were surrounded by Iba1+ microglia
419 with a distinct morphology (fig. **5e,f**). A second experiment revealed these *C3*+ foci
420 were also *Slc1a3*+ indicating these foci were reactive astrocytes (fig. **5g-i** & **S7a,b**).
421 In HP1β/γ DKO hippocampi, the number of total GFAP+ astrocytes significantly

increases compared to young DKO animals, although this puts it in the same range as the other genotypes. Notably, ~50% more Iba1+ microglia can be observed in aged HP1β/γ DKO hippocampi (fig. **5j,k** & **S7c,d**). We could observe the Iba1+ microglia neighboring GFAP+ astrocytic foci in the *stratum radiatum* of HP1DKO hippocampi exhibited large CD68+ protrusions (arrows fig. **5l**), indicating augmented phagocytosis. We quantified the CD68+ area within Iba1+ cells and found that this significantly increased in HP1β/γ DKO hippocampi in an age-dependent manner (fig. **5m**). This suggested that pro-inflammatory signalling, likely as a result of the de-repression of IAPs and other ERVs, chronically results in greater activation of microglia.

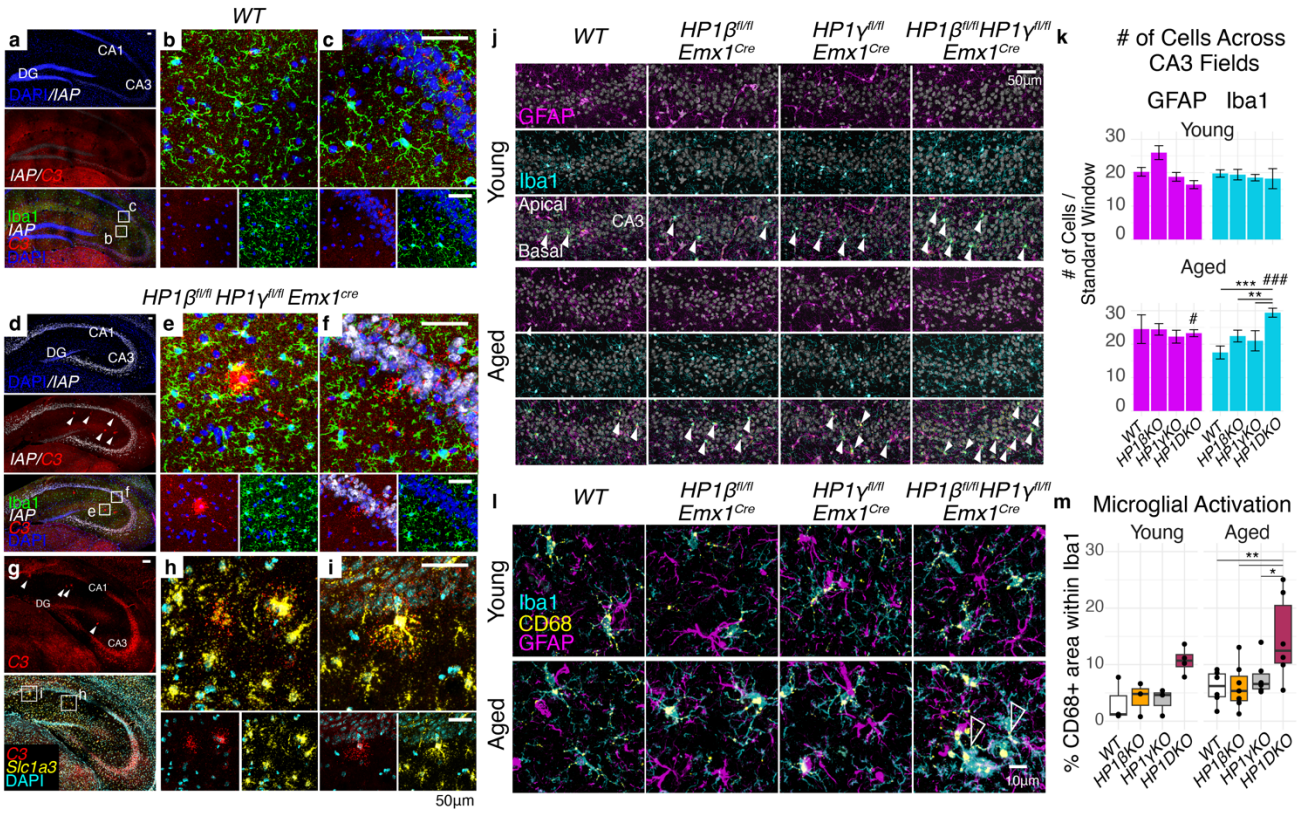

Figure 5. Chronic de-repression of ERVs coincides with the appearance of C3+ reactive Astrocytes and increased CD68+ Microglia. Moderate Complement 3 (C3) RNA can be detected by RNAscope in aged WT **a-c**, where it can be detected in most cells of the hippocampus including CA1 and CA3 pyramids. (Representative images are displayed here after testing across 3 brains per condition). De-

repression of IAP transcripts in aged *HP1β*$^{fl/fl}$*HP1γ*$^{fl/fl}$*Emx1*^{Cre} (white, **d**) corresponds with large C3+ islands (arrows in **d**) that can be found in the *Stratum Radiatum* (magnified in **e**) and emanating from the *Stratum Pyramidale* (magnified in F). Such C3 foci are surrounded by microglia with distinct morphology (compare **b** & **c** to **e** & **f**). C3+ foci found in the *Stratum Radiatum* of *HP1β*$^{fl/fl}$*HP1γ*$^{fl/fl}$*Emx1*^{Cre} hippocampi are Slc1a3+ astrocytes (**g**, magnified in **h** & **i**). **j** Representative images of CA3 pyramidal layers stained for GFAP, Iba1 and Dapi. Iba1+ cells entering the *stratum pyramidale* are indicated with solid arrows. **k** Quantification of GFAP+ and Iba1+ cells across apical, somal, and basal regions in CA1 and CA3 fields (see also fig S7). Statistics two-way ANOVA with estimated marginal means post-hoc test with Tukey's familywise correction. Young: WT n= 8, HP1βKO n = 10, HP1γKO n=8, HP1DKO n=10, Aged WT n=8, HP1βKO n= 14, HP1γKO n=8, HP1DKO n= 14. Adjusted p values for genotype test within age (Iba1): aged HP1DKO vs WT p=0.003, aged HP1DKO vs aged HP1γKO p=0.0152, aged HP1DKO vs aged HP1βKO p = 0.0152. Adjusted p values for age test within genotype: Iba1 HP1DKO age p<0.0001, GFAP HP1DKO age p = 0.0087. **l** Iba1+ microglia that can be found in the *stratum radiatum* surrounding GFAP+ astrocytes contain large CD68+ compartments suggesting endosomal activity. **m** Quantification of Microglial activation (from **l**) measured by the proportion of CD68+ area within Iba1+ microglia. Statistics two-way ANOVA with estimated marginal means post-hoc test with Tukey's familywise correction. Young: WT n= 3, HP1βKO n = 3, HP1γKO n=3, HP1DKO n=4, Aged WT n=6, HP1βKO n= 7, HP1γKO n=6, HP1DKO n= 6. Adjusted p values for genotype test within age: aged HP1DKO vs WT p=0.008, aged HP1DKO vs aged HP1γKO p= 0.0444, aged HP1DKO vs aged HP1βKO p = 0.0064.

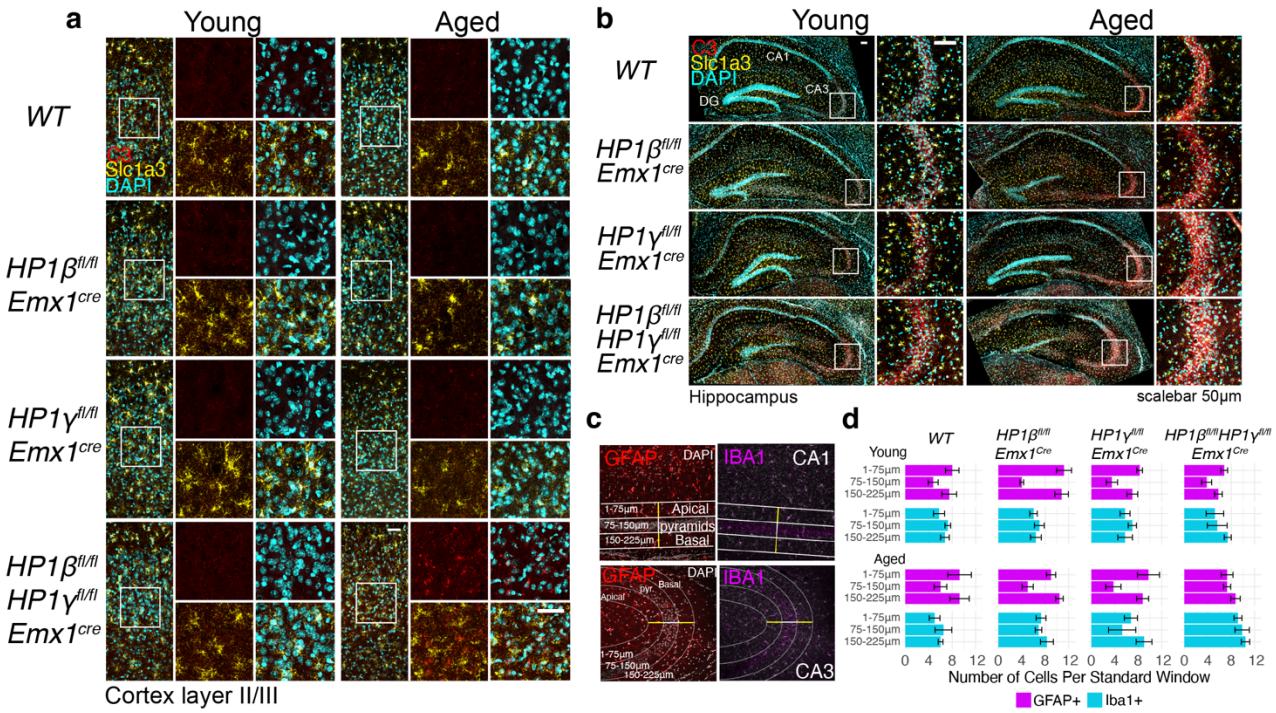

Figure S7. Initiation of Complement and invasion of microglia in HP1DKO cortices and hippocampi. Multiplex In situ hybridization using probes for *C3* and *Slc1a3* in the cortex (**a**) and hippocampus (**b**) of young and aged HP1 mutants. Distribution of astrocytes and microglia in or adjacent to pyramidal layers of the hippocampus. **c** Quantification scheme for CA1 and CA3 fields. Iba1+ microglia and GFAP+ cells with astrocyte morphology were quantified with 75 μm bins in standard windows across apical, pyramidal and basal fields. For CA1, straight lines separated by 75μm equivalent pixels was used, whereas for CA3, standard ellipses separated with 75μm equivalent pixels were used. Quantification summary of GFAP+ and Iba1+ can be seen by bin in **d** and across all fields in figure **5m**.

While it is known that proteins derived from ERVs can be pro inflammatory in the brain[47], the majority of ERV transcripts do not have complete coding sequences. Given that IAP transcripts de-repressed in *HP1β*$^{fl/fl}$/*HP1γ*$^{fl/fl}$*Emx1*^{Cre} brains are neuronally derived and glial activation follows, we designed an experiment to profile the stimulatory effect of IAP ssRNA on mixed glial cultures *in vitro* (fig **6a**). As a control, we used the same sequence derived from IAP but substituted pseudo uracil[48], thus termed ψ-IAP (fig **6b**). Twenty-four hours following introduction of IAP ssRNA we profiled the media and cytosolic lysate for activation of chemokines and

486 cytokines using a membrane-based sandwich immunoassay (fig **6c**). We found
487 robust activation of several classical cytokines in response to IAP ssRNA including
488 TNF, IL-6, IL-12, IL-16, IL-23 (fig **6d**). The most prominent activation was in CCL3,
489 CCL4 and CCL5 (RANTES). We confirmed CCL5 activation predominantly came
490 from GFAP+ astrocytes (fig **6e**) and this was specific to IAP ssRNA and not ψ-IAP
491 ssRNA (fig **6f**). Interestingly, while IFN-γ increases were not statistically significant
492 in our assay, the cytokine response to IAP ssRNA observed here are consistent with
493 previous observations of IFN-γ stimulated increases of ERV dsRNA, which includes
494 elevated IL-6 and CCL5[49].

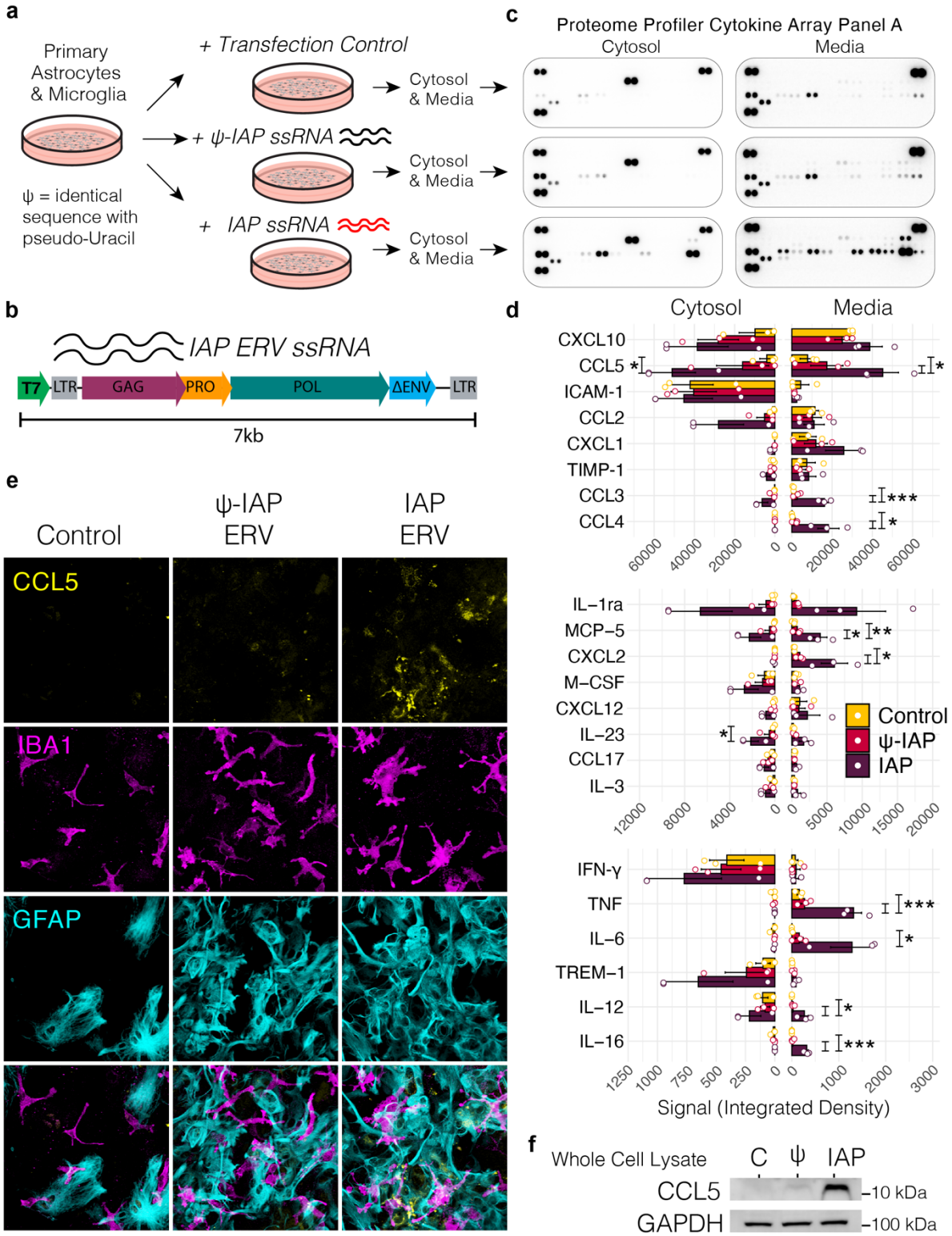

Figure 6. Acute introduction of IAP ssRNA induces an inflammatory response. **a** Schematic showing experimental design where primary astrocytes and microglia are exposed to a pulse of regular- or pseudo (ψ)- IAP ssRNA, where ψ-IAP is generated from the same template but with ψ-uracil. **b** Full length IAP template used for generation of ssRNA. **c** Representative dot plots from Proteome Cytokine Array Panel A following incubation with media or cytosolic lysates from control, ψ-

502 IAP ssRNA or IAP ssRNA treated glial cultures. **d** Quantification of Cytokine Panel A
503 immunoassays, performed in 3 biological replicates separated by cytosol and
504 media, split by high signal (top), medium signal (middle), and low signal (bottom).
505 **e** Immunofluorescence stain of glial culture comprised of Iba1+ microglia and
506 GFAP+ astrocytes stained for CCL5 (RANTES) and GAPDH loading control following
507 incubation with ψ-IAP and IAP ssRNA.

508

509

510 **Increased Dendritic loss and Cognitive Decline**

511 Young HP1β KO CA3 hippocampal neurons showed a modest reduction in
512 CA3 basal dendrite complexity that was carried through to aged animals. By
513 contrast, HP1β/γ DKO animals displayed a pronounced age-dependent decrease
514 in CA3 basal dendrite complexity (fig. **7a**). Structural MRI revealed that while young
515 HP1β/γ DKO animals have a modestly reduced volume of both the cortex and total
516 brain, this difference is less obvious in aged HP1β/γ DKO animals (fig. **S8**).

517 Cognition and behavior of HP1 mutant mice was profiled as young adults (3-
518 4 months) and again in middle age (13-14 months), where we observed several age-
519 dependent deficits. HP1β/γ DKO animals exhibited deficits in spatial learning and
520 memory as tested in the Barnes maze (fig. **7b**). Young HP1β/γ DKO animals showed
521 impairment in both learning (24h test) and recall (7 day test) of the target nest, while
522 aged HP1β/γ DKO animals seemed unable to learn the location of the target nest
523 and typically walked around the periphery continuously. Aged HP1β/γ DKO
524 animals also showed an age-dependent abolition of paired-pulse inhibition (fig.
525 **S9a**), extended bouts of eating and grooming (fig **S9b**) and an altered circadian
526 rhythm (fig. **S9f**). During handling and testing, a subset of HP1 mutant animals
527 displayed stimulus-dependent seizures, which were observed with HP1β KO
528 animals predominantly (fig. **S9e**). Young HP1β/γ DKO animals displayed
529 hyperactivity in an open field, and as aged animals they showed both an absence

530 of center zone anxiety (fig. **S9c**) and a marked inability for nest construction (fig.
531 **S9d**).

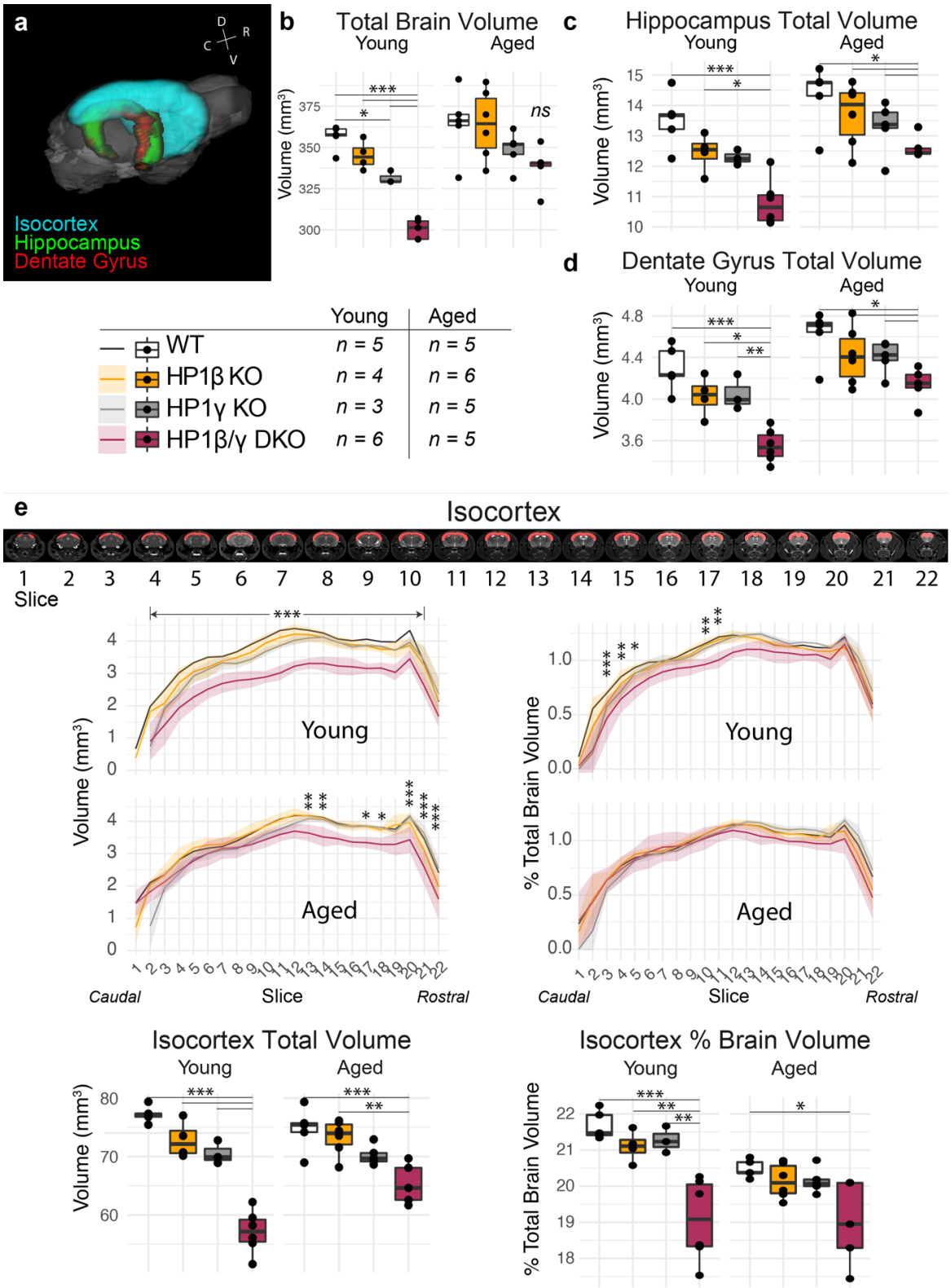

532

533 **Figure S8.** Structural Magnetic Resonance Imaging of HP1 mutants. **a** Registration
534 of Isocortex, Hippocampus and Dentate Gyrus. Absolute volumes of total brain **b**,

Hippocampus **c** and dentate gyrus **d** in young and aged HP1 mutants. **e** Slice-wise depiction of isocortical volume, both absolute (left) and as a percentage of total brain volume (right). All animals were included in the analysis. Statistics: one-way ANOVA within age with Bonferroni multiple comparison corrections. *** = $p < 0.001$, ** = $p < 0.01$, * = $p < 0.05$.

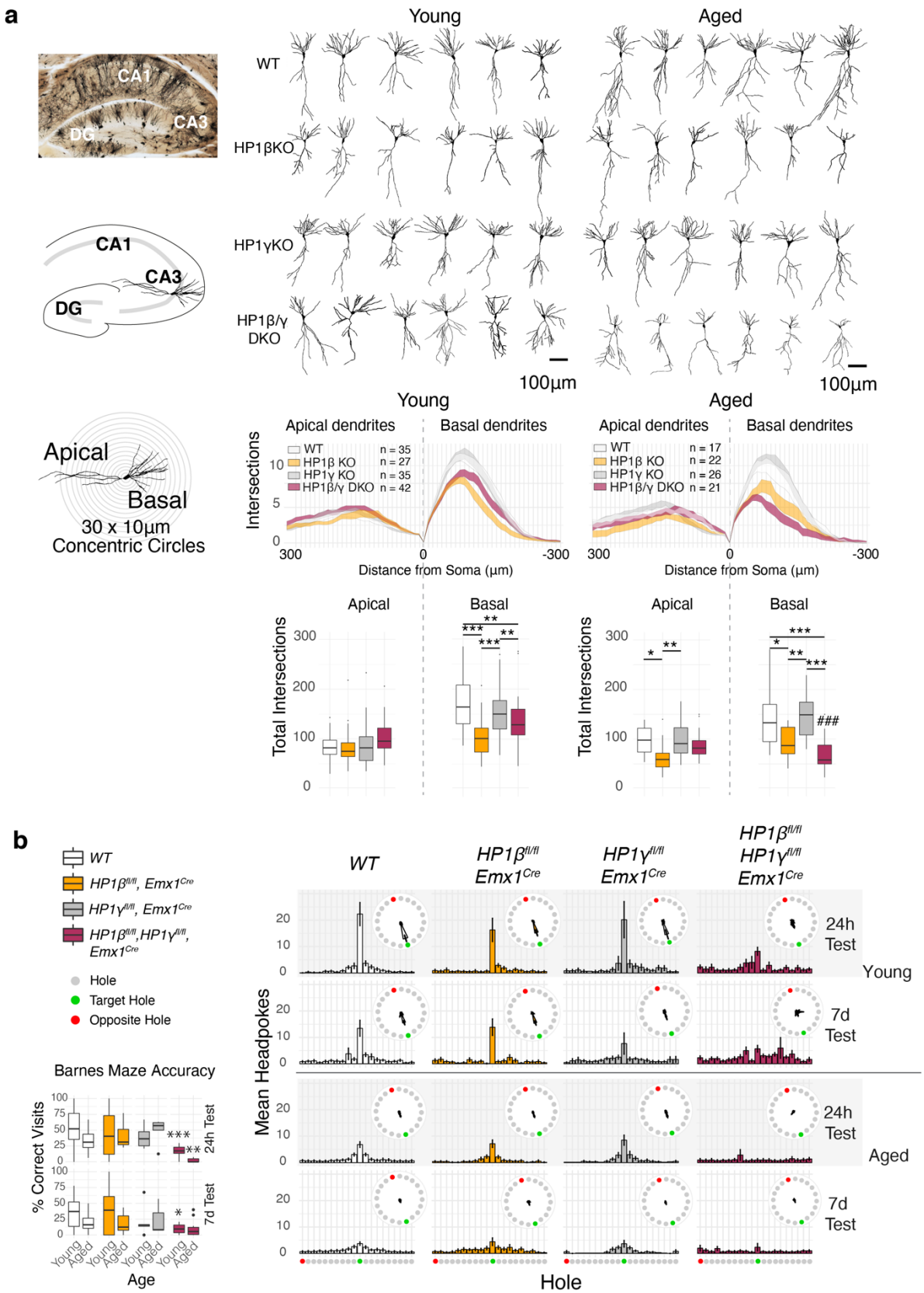

Figure 7. HP1 deficiency causes age related behavioral abnormalities and CA3 dendritic tree degeneration. **a** CA3 Dendritic Complexity in young and aged HP1 mutants by Golgi impregnation and Scholl analysis. Deficits in basal dendrite

complexity can be observed in young HP1βKO and HP1β/γ DKO animals. While basal dendrite complexity is nearly identical in aged HP1βKO, HP1β/γ DKO basal dendrites show an age dependent degeneration, losing almost 50% of their complexity. **b** Histograms of performance in the circular Barnes Maze (green = target hole, red = opposite). Histograms plot mean headpokes ±SEM. Asterisks mark ANOVA across genotypes within age, *** $p < 0.001$, ** $p < 0.01$, * $p < 0.05$. Hashtags mark ANOVA across age within genotype, ### $p < 0.001$.

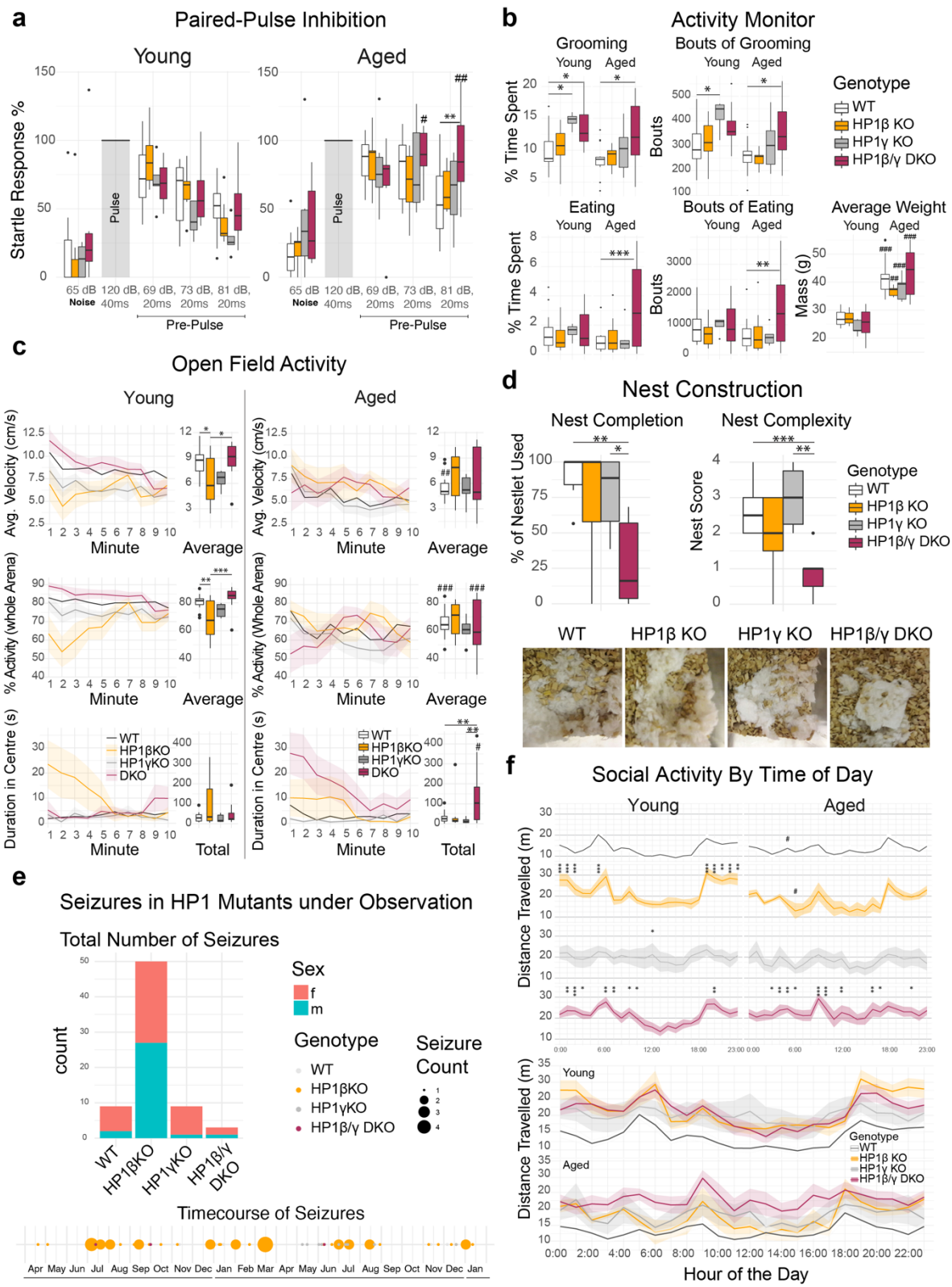

Figure S9. Age-related changes in behavior in HP1β/γDKO animals. **a** Paired-Pulse Inhibition recordings across HP1 mutants. All paired startle responses are percent normalized to the amplitude of the startle pulse (120dB) alone. A strong age-dependent change in paired pulse inhibition was seen in HP1β/γDKO

558 animals, where pre-pulses of larger amplitude failed to further attenuate a startle
559 response. **b** Altered Grooming, Eating and Circadian Activity in HP1mutants.
560 HP1DKO animals showed an increased total time and frequency of grooming, and
561 aged HP1DKO also displayed higher bouts of eating, though this did not translate
562 into an increase in weight. Anxiety and exploration measured in an open field test
563 revealed age dependent delays in HP1DKO animals (**c**). Young HP1βKO animals
564 displayed non-convulsive freezing responses upon placement in the chamber
565 which bias their measurements. **d** Nest construction profiled in aged animals was
566 scored based on nest completion (% Nestlet used) and nest complexity (standard
567 rubric, see methods) show marked deficits in HP1DKO animals. **e** Seizures
568 observed in HP1 animals occurred predominantly in HP1β KO animals and were
569 typically stimulation dependent, where observed seizures were non-randomly
570 distributed, often occurring because of standard cage changes. Social activity **f** of
571 mice observed over a 14 day period binned by hour reveals general hyperactivity
572 in HP1βKO and HP1β/γDKO animals as well as an age-dependent change in peak
573 nocturnal activity. Statistics are two-way ANOVA with Bonferroni correction on
574 multiple comparisons; Asterisks (*) denote tests to wildtype within age, hashtags
575 (#) denote tests within genotype between age.
576

577 **Discussion**

578 Our study has uncovered nonredundant functions of HP1β and HP1γ in
579 neurons. The age-dependent reduction in DNA methylation at imprinted loci as
580 observed for *Nnat* in *HP1β*$^{fl/fl}$*Emx1*^{Cre} indicates that HP1β stimulates Dnmt1 activity,
581 as has been described previously[50]. That the two proteins can operate along the
582 same pathway would explain the similarity of the reduction in the formation of the
583 dentate gyrus in tamoxifen induced *Nestin-Cre* deletion of *Dnmt1*[51] compared to
584 that observed here with *HP1β*$^{fl/fl}$*Emx1*^{Cre}. Moreover, the robust activation of IAP
585 elements in *Dnmt1*$^{fl/fl}$*Emx1*^{Cre} mutant phenocopies the *HP1β*$^{fl/fl}$*HP1γ*$^{fl/fl}$*Emx1*^{Cre}
586 mutant, albeit the *Dnmt1*$^{fl/fl}$*Emx1*^{Cre} mutant also displays a dramatic malformation of
587 the cortex [52], which we did not observe. Notably, many of the genes upregulated
588 in *HP1β*$^{fl/fl}$*HP1γ*$^{fl/fl}$*Emx1*^{Cre} hippocampi overlap with regions where Dnmt1-
589 dependent methylation is not recovered once abolished [53]. Since 5mC methylation
590 is dramatically lost at ERVK elements in *HP1β*$^{fl/fl}$*HP1γ*$^{fl/fl}$*Emx1*^{Cre} but not in single
591 mutants, this suggests that *HP1β or HP1γ* are capable of stimulating Dnmt1 activity

592 and the loss of both is detrimental. Age-related 5mC hypomethylation appears to
593 be restricted to loci already under threat of activation such as the tissue-specific
594 imprinted genes (*i.e., Nnat*) or partially silenced ERVK repeats such as IAPs. This
595 phenomena has been observed before with IAP elements in aging mice—where
596 their periodic activation results in progressive demethylation and complete de-
597 silencing [54], and may explain why IAP transcription further increases in aged
598 *HP1β*$^{fl/fl}$*HP1γ*$^{fl/fl}$*Emx1*^{Cre} (fig. **1c**). The shift towards hydroxymethylation in
599 *HP1β*$^{fl/fl}$*HP1γ*$^{fl/fl}$*Emx1*^{Cre} hippocampi along with the measured increases in age-
600 related hydroxymethylation in non-coding regions (fig **4e**) indicate that HP1
601 proteins also serve to protect against TET-mediated hydroxymethylation.

602 *HP1β*$^{fl/fl}$*HP1γ*$^{fl/fl}$*Emx1*^{Cre} hippocampi show several functional similarities with
603 the transcriptional signatures of very aged (24-29 month) mouse hippocampi. Very
604 aged hippocampi display downregulation of ZFP57, Suv420h2, and upregulation
605 of much of the protocadherin cluster [55]. Some of the strongest transcriptional
606 changes in *HP1β*$^{fl/fl}$*HP1γ*$^{fl/fl}$*Emx1*^{Cre} hippocampi are also the strongest observed
607 changes in very aged hippocampi, including age-associated ncRNAs *Pisd-ps1* and
608 *Pisd-ps2* and complement components *C1qa, C3*, and *C4b* [46,55–57].

609 *HP1β*$^{fl/fl}$*HP1γ*$^{fl/fl}$*Emx1*^{Cre} hippocampi also show similarities to the 'pre-plaque'
610 state[58]. According to current concepts, the mechanism by which astrocytes and
611 microglia co-ordinate the complement cascade involves the initial activation of
612 microglia. Activated microglia then secrete Il-1a, TNF and C1q that induce A1-
613 astrocyte reactivity [59]. In addition to being directly neurotoxic [59], it is thought
614 reactive astrocytes also greatly enhance the susceptibility of aging brains to
615 neurodegeneration because they are major source of classical complement
616 cascade components C3 and C4b that then drive microglia-mediated synapse loss
617 [58]. In Alzheimer's disease, microglial activation and synapse loss precedes plaque
618 pathology in the hippocampus [58], and reactive astrocytes have long been
619 associated with senile amyloid plaques (for review see [60]).

620 Although it is unclear how microglia are activated in *HP1β*$^{fl/fl}$*HP1γ*$^{fl/fl}$*Emx1*^{Cre}
621 hippocampi, a likely sequence of events is that microglia activation is a response to
622 the export of ERV or other inflammatory RNA from *HP1β*$^{fl/fl}$*HP1γ*$^{fl/fl}$*Emx1*^{Cre} neurons
623 that is detected by astrocytes and microglia. Similar export of RNA or protein-
624 aggregate filled extracellular vesicles (EVs) have been observed in neuron-neuron
625 or neuron-glia communication [61,62], and ERVs have been shown to be included in
626 EVs [63]. In this context, human ERVs have been found to be elevated in Alzheimer's
627 [17] and ALS [20]. Extracellular vesicles that export neuronal unfolded protein
628 aggregates have also been shown to serve as an activating signal to microglia or
629 astrocytes [62] and this is sufficient to drive non-cell-autonomous neuronal
630 degeneration [64].

631 When we tested the effect of extracellular ERV RNA on mixed glial cultures,
632 we could observe an inflammatory response akin to direct stimulation of IFN-γ [49],
633 which is also consistent with the upregulation of a large number of interferon related
634 genes we observed in RNaseq (fig. **1**). We also note the upregulation of IFNGR2,
635 the regulatory subunit[65] of the interferon gamma receptor in *HP1β*$^{fl/fl}$*HP1γ*$^{fl/fl}$*Emx1*^{Cre}
636 hippocampi. Activated astrocytes in many neurodegenerative diseases show
637 upregulation of IFNGRs[66], suggesting an increase in sensitivity to IFN-γ signaling.
638 Once effected, IFN-γ signaling has been observed to up-regulate expression of the
639 complement components C3 and C4 by stabilization of their mRNA [67,68]. Notably,
640 in addition to other non-inflammatory roles, IFN-γ signaling has been shown to
641 promote tau hyperphosphorylation [69].

642 The extensive cross-talk that occurs between innate immune pathways and
643 the unfolded protein response (UPR) is known collectively as the integrated stress
644 response (ISR) [70]. UPR engagement in *HP1β*$^{fl/fl}$*HP1γ*$^{fl/fl}$*Emx1*^{Cre} hippocampi is likely
645 a direct result of sustained ERV transcription. It is known that extended UPR stress
646 in astrocytes results in Complement Activation[64] . Our results are also consistent
647 with observations that TDP-43 proteinopathies, which can be potentiated by

648 elevated ERV expression[22], also result in activation of complement[71]. Given the
649 majority of neurodegenerative diseases are characterized by misfolded proteins or
650 altered proteostasis [70,72], this provides an invaluable insight into how
651 heterochromatin loss alone can drive core components of neurodegeneration[73]
652 and accelerated cognitive decline.

653 Complement activation in the aging brain may have as many exogenous
654 inducers as there are pathways to inflammation. However, the present study
655 indicates that at least one primary trigger of the innate immune response is of
656 endogenous origin: namely, the activation of endogenous retroviruses following
657 heterochromatin loss.

658

659

660

661 **Acknowledgments:** Computation was performed on the HPC for Research/Clinic
662 cluster of the Berlin Institute of Health. We would like to acknowledge Julie
663 Brind'Amour, Carol Chen and Matthew Lorincz for early discussions. We thank
664 Marion Rivalan and Melissa Long from the NeuroCure Animal Outcome Core
665 Facility (AOCF) for facilitating behavioral experiments. We thank Robert Schwarz
666 for statistical advice on calculating Odds Ratios. We also thank Seija Lehnardt and
667 Christina Krüger for advice with astrocyte culture. We would also like to thank
668 Ingo Bormuth, Roman Wunderlich, Ulrike Günther, Denis Lajkó and the animal
669 facility of the Charité.

670

671 **Funding:** This work was supported by DFG research grant 410579311 (A.G.N &
672 V.T.); Funding to S.Z was provided by the German Research Foundation (DFG,
673 SFB665, SFB1315), and the German Academic Exchange Service (DAAD); Funding
674 to P.B-S. was provided by the German Federal Ministry of Education and Research
675 (BMBF) under the ERA-NET NEURON scheme (01EW1811) and the DFG (research
676 grant BO 4484/2-1). Research by PBS was supported by a Nazarbayev University
677 Faculty Development Grant 021223FD8818 and by the Ministry of Health of the
678 Republic of Kazakhstan under the program-targeted funding of the Ageing and
679 Healthy Lifespan research program (IRN: 51760/ПЦФ-М3 РК-19).

680 **Author contributions:** Conceptualization, A.G.N, P.B.S and V.T.; Investigation,
681 A.G.N., J.S., S.Z., P.B., S.M., P.B-S.; Resources, A.G.N., J.B., M.N., O.O., H.K.;
682 Bioinformatics, A.G.N.; Formal analysis, A.G.N.; Visualization, A.G.N.; Funding

683 acquisition, A.G.N., P.B.S., V.T.; Writing-original draft, A.G.N., Writing-review and
684 editing, A.G.N., P.B., P.B.S., V.T., Writing-revision A.G.N.; All authors reviewed the
685 final manuscript.

686 **Competing interests:** Authors declare no competing interests.

687 **Data availability:** Data from this study has been deposited at GEO under
688 accession # GSE153331

689 **Code availability:** Code used in analysis can be accessed at
690 https://github.com/qoldt/HP1-Deficiency-Neurodegeneration

691

692 **Methods:**

693

694 **Mouse Lines**

695 All animal experiments were conducted in compliance with animal welfare
696 guidelines put in place by the für Gedundheit und Soziales (LaGeSo) Berlin.

697 The **H**eterochromatin **P**rotein **1** **F**loxed **E**mx1**C**re (HP1FEC) mouse line was
698 generated by generating floxed alleles of HP1β (*Cbx1*) and HP1γ (*Cbx3*) which
699 were combined with the Emx1-IRES-Cre mouse (Jackson Laboratory). The HP1β
700 (*Cbx1*) targeted allele was generated by introduction of a targeting cassette into
701 ES cells by homologous recombination that inserted loxP sites surrounding exons
702 II and III. Successful integrations were detected by neomycin selection via an FRT
703 flanked neomycin cassette inserted between exons III and IV. Following a cross to
704 a flip-deleter mouse, the NeO cassette is removed by flippase-mediated
705 recombination, giving rise to the $HP1\beta^{fl/fl}$ allele (Figure S10). HP1γ (*Cbx3*) was
706 targeted using a similar strategy giving rise to the $HP1\gamma^{fl/fl}$ allele (Figure S11).

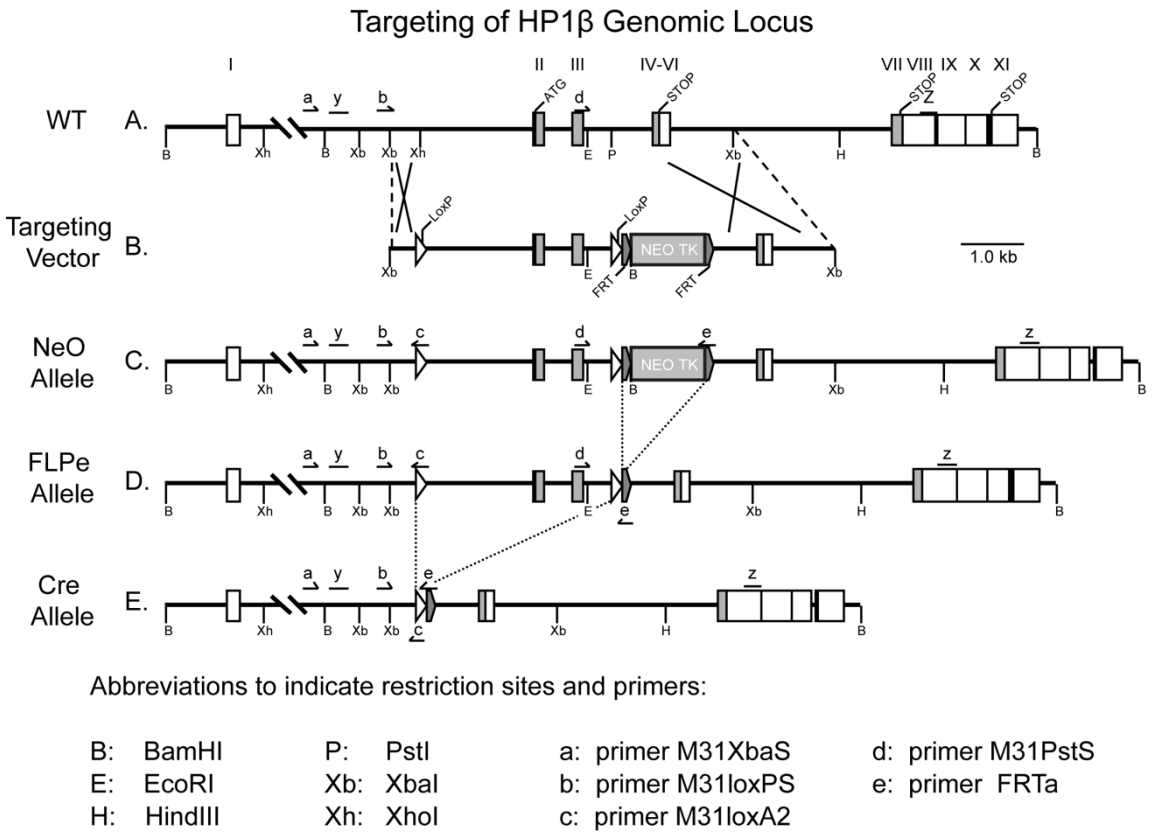

Extended Data Figure S10. Targeting of Cbx1 (HP1β) genomic locus.

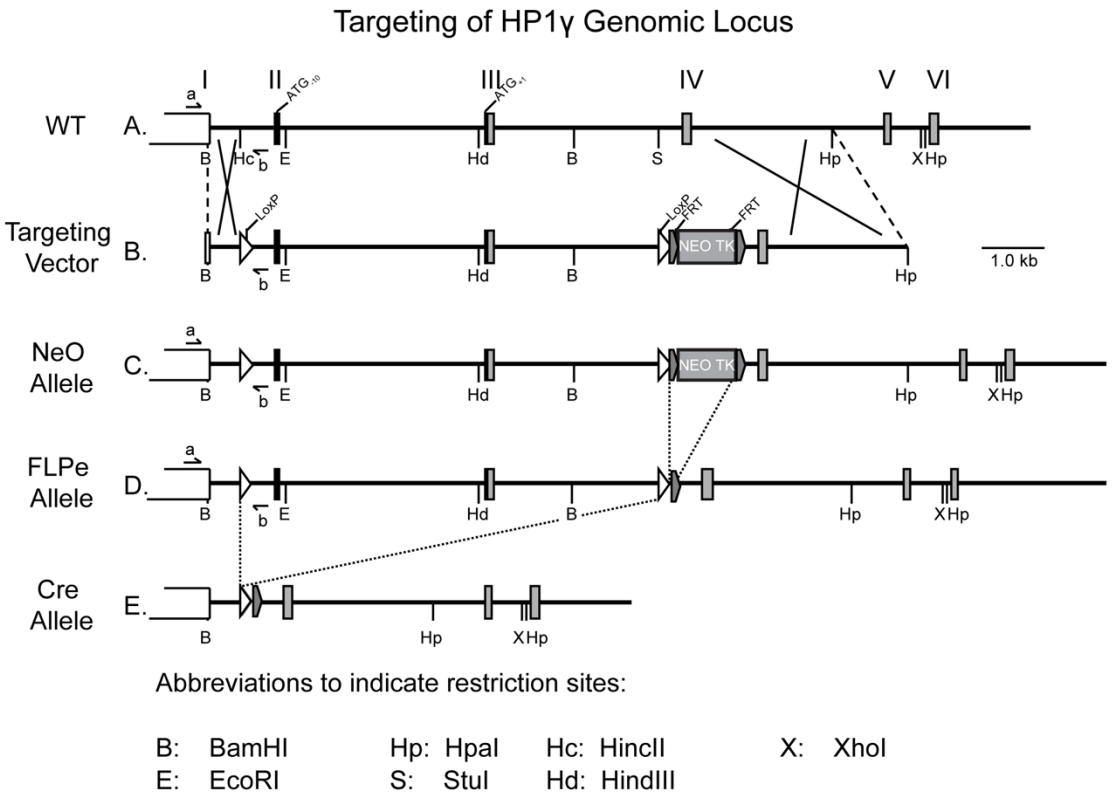

Extended Data Figure S11. Targeting of Cbx3 (HP1γ) genomic locus.

HEK Cell Culture & Transfection

HEK293T cells were cultured in DMEM+Glutamax (Gibco) supplemented with 10% FBS and 1% penicillin/streptomycin (Gibco). For Co-IP experiments, HEK293T cells were seeded in 6 well plates at a density of 0.3 x 10^6 cells per well. For IHC, cells were plated onto glass coverslips in 24 well plates at 100,000 cells per well. Plasmid DNA was introduced into cells by chemical transfection using Lipofectamine 2000 according to the manufacturer's instructions.

Co-Immunoprecipitation (Co-IP) and Western Blot (WB)

Six well plates were rinsed briefly in cold PBS, then lysed on ice in 300µl of Radioimmunoprecipitation assay buffer (RIPA, 50 mM Tris, pH 8.0, 150 mM NaCl, 1% Triton X-100, 0.5% Sodium Deoxycholate, 0.1% SDS) supplemented with 1X Protease Inhibitor Cocktail (PIC, Roche). Lysates were then sonicated for 15 pulses

728 on ice using a probe sonicator. Insoluble debris was then precipitated by
729 centrifugation at 13,000 rpm at 4°C, and then decanted into a new tube.
730 Protein concentration was measured using a standard Bicinchroninic acid
731 (BCA) assay, by using 10µl of protein sample diluted 1:10, plating 25µl into a 96
732 well plate in triplicate along with a Bovine Serum Albumin (BSA) standard (0, 0.1,
733 0.2, 0.5, 0.75, 1.0, 1.5, 2.0 µg/µl).
734 Prior to immunoprecipitation, each sample was adjusted to a 300µl volume
735 at a protein concentration of 1.5 µg/µl using lysis buffer, and 20µl of lysate was set
736 aside for input. To perform the immunoprecipitation, 1.5µl of antibody (mouse
737 anti-myc 9B11, Cell Signaling or goat anti-GFP, Rockland) was incubated per
738 sample on a rocker for 2 hours at 4°C. During this time, protein G sepharose
739 beads (GE Healthcare, 25 µµl per sample) were rinsed 3 x 15 minutes in 1ml of
740 cold TBS (50 mM Tris pH 7.5, 150 mM NaCl), rocking at 4°C. Between washes
741 beads were spun down using a short 5 second spin on a tabletop centrifuge (no
742 greater than 9,000 rpm). Following the 2 hour antibody/lysate incubation, washed
743 beads are added to each sample and incubated on a rocker for an additional hour
744 at 4°C. Following IP, beads are washed twice using lysis buffer and twice with TBS.
745 On the final wash, as much buffer was removed as possible before addition of
746 25 µµl 2.5X lammeli buffer. IP was then boiled at 95°C for 5 minutes. For input
747 samples, 5 µµg of total lysate was used in a volume of 25 µµl, adjusted with 5 µµl
748 5X lammeli buffer and the appropriate amount of lysis buffer, and boiled at 95°C
749 for 5 minutes.
750 **RNA Isolation**
751 For cDNA library construction, RNA was purified from P0 cerebral cortices
752 using TRIzol (Invitrogen) according to the manufacturer's instructions followed by
753 reverse transcription by SuperScript II (Thermo Fischer) using random primers.
754 For RNAseq, RNA was isolated using the Relia-prep RNA mini kit (Promega)
755 according to the manufacturer's instructions.

756 **RNAseq Library Preparation**

757 RNA-seq libraries were prepared with the NEBNext Ultra RNA Library Prep
758 Kit for Illumina (New England Biolabs), using 1 µg total RNA per experiment.

759 **Molecular Cloning**

760 For in situ probes, primers were designed around consensus sequences
761 obtained from repbase (https://www.girinst.org/repbase/) and amplicons were
762 queried using UCSC's BLAT and in silico PCR tools to determine the estimated
763 diversity of transcripts corresponding to the probe. Probe primers for a unique
764 IAP element on chr 2 were inferred based on unpublished qPCR primers (Julie
765 Brind'Amour, UBC) (Data S1). Probe sequences were amplified from cDNA using
766 GoTaq Polymerase (Promega) and ligated into the pGEM®-T vector (Promega).
767 Linearized plasmids were then used as templates for in vitro transcription using
768 either SP6 or T7 (Roche) using DIG labelled nucleotides (Roche). Following DNA
769 digestion and RNA purification, the RNA probe was resuspended in 20µl water
770 and 180µl hybmix (50% formamide, 5X SSC pH 7.0, 1% Boehringer block, 5mM
771 EDTA, 0.1% Tween-20, 0.1% CHAPS, 0.1 mg/ml Heparin, 100 µµg/ml Yeast tRNA)
772 and stored at -20°C until needed.

773 To clone HP1 and SUV420H2 expression constructs, two rounds of PCR
774 were conducted using the high fidelity Q5 Polymerase (New England Biolabs).
775 The first round of PCR amplified the 'naked' coding region of the gene (*_110 and
776 *_111 primers), and using this product as a template, a second PCR was
777 performed with primers removing the stop codon and containing restriction sites.
778 These amplicons were then A-tailed using GoTaq polymerase (Promega) and
779 ligated into the pGEM®-T vector (Promega) yielding pGEMT-KnpI-HP1x (where x is
780 α, β, or γ). To generate eGFP fusions, inserts were digested with KpnI and AgeI for
781 insertion into pCAG-eGFP (Clontech), yielding pCAG-HP1x-GFP fusion constructs.
782 Prior to cloning SUV420H2, pCAG-mycDKK was created by substituting the CAG
783 promoter from pCAG-eGFP with the CMV promoter of pCMV6-Entry though

784 digestion with SpeI and EcoRI. First, 'naked' SUV420H2 was amplified using 110
785 and 111 primers, then 1µl of this template was used for a PCR using kpnI and XhoI
786 primers. The KpnI-SUV420H2-XhoI PCR product was then gel-extracted and
787 digested for 20 minutes using Fast Digest KpnI and XhoI (Fermentas) and
788 subsequently ligated into KnpI/XhoI digested pCAG-mycDKK, resulting in an in-
789 frame C-terminal myc-DKK (Myc tag and Flag tag).
790 For SUV420H2/HP1 IP experiments, mutations were created in the
791 chromoshadow domain of HP1γ in pGEMT-KpnI-HP1γ using the Q5 site-directed
792 mutagenesis kit (New England Biolabs) according to manufacturer's instructions
793 (Data S1). Following sequence verification, mutant HP1γ inserts were ligated into
794 pCAG-eGFP as above. Expression plasmids from this study have been deposited
795 at https://www.addgene.org/browse/article/28223393/ .
796 For cloning of the full length IAP construct for in vitro transcription, pFL , a
797 plasmid encoding full length IAP [74] and kind gift of Prof. Horie, was first subcloned
798 to delete the antisense intronic GFP using a NEB KLD reaction, and then a T7
799 promoter sequence was added 5' to the LTR by NEBuilder gateway cloning,
800 resulting in the plasmid pT7-IAP. Primers can be seen in Data S1.
801 **In vitro transcription of IAP ssRNA**
802 The pT7-IAP plasmid was linearized using NaeI and NotI for 4 hours at 37°C
803 using 15ug of plasmid DNA. The linearized 6.8kb fragment was then gel purified &
804 used as a template for in vitro transcription (IVT) using the RiboMax large scale RNA
805 production system (Promega, cat # P1300) with minor modifications. First, 3'
806 overhangs were filled in by incubating 10ug of DNA template with DNA polymerase
807 I large (Klenow) Fragment in T7 transcription buffer for 15 minutes at 22°C. Then
808 T7 in vitro transcriptions were set up with rNTP mixes. For IAP RNA a normal mix of
809 rNTPs (100mM ATP, 100mM UTP, 100mM CTP, 100mM GTP), and for pseudo-IAP,
810 pseudo-uracil was substituted (100mM ATP, 100mM Ψ-UTP, 100mM CTP, 100mM
811 GTP). IVT reactions were then incubated with T7 & respective rNTP mixes for 4hrs

812 at 37°C. Following in vitro transcription, RQ1 RNase-free DNase was added at a
813 concentration of 1u per µg of template DNA and incubated for 15 minutes at 37°C.
814 Then, RNA was extracted in the aqueous phase after addition of 1 volume of citrate-
815 saturated phenol (pH 4.7):chloroform:isoamyl alchohol (125:24:1) (Sigma, cat #
816 77619), and a second addition of 1 volume of chloroform:isoamyl alcohol (24:1).
817 The aqueous phase was then transferred NAP-5 (GE Healthcare Cat# 17-0853-01)
818 chromatography columns for the removal of unincorporated ribonucleotides and
819 eluted using ultrapure RNase free water. RNA was then precipitated by addition of
820 0.1 volume of 3M Sodium Acetate (pH 5.2) and 1 volume of isopropyl alcohol,
821 mixing well and incubating 5 minutes on ice. Precipiated RNA was then pelleted by
822 centrifugation at 13,000 in a tabletop centrifuge at 4°C. Supernatant was then
823 discarded and the RNA pellet washed in 70% ultrapure EtOH, dried & resuspended
824 in a volume of Ultrapure ddH2O equal to the transcription reaction. RNA
825 concentration was then measured by first diluting 2µl of RNA into 298µl of water
826 and measuring the absorbance at 260nm. The concentration of RNA was then
827 calculated using the expression

828 $$C = (A_{260nm} * dilution\ factor)\ /\ (10{,}313\ x\ nucleotides)$$

829 where C is in moles and the dilution factor is 100. In vitro transcribed RNA was then
830 confirmed by denaturing 1µg of RNA at 65°C for 10 minutes in 1.5X probe buffer
831 (60% formamide, 40% glycerine 6% formaldehyde, 5% ethidium bromide, 5%
832 bromophenol blue, 20mM MOPS, 5mM EDTA, 2.1mM Calcium Acetate) and
833 running on a 1% agarose gel (20mM MOPS, 5mM EDTA, 2.1mM Calcium Acetate,
834 6% formaldehyde, 1 % agarose) using MOPS (20mM MOPS, 5mM EDTA, 2.1mM
835 Calcium Acetate) as the running buffer.
836

837 **Transfection of Primary Astrocytes & Microglia for Cytokine Profiling**

838 Astrocytes and microglia were obtained by trypsin-assisted dissociation of
839 P0 cortices and cultured for two weeks in DMEM supplemented with 10% FBS and

840 1% penicillin/streptomycin. Mixed glia were then seeded on poly-D-lysine coated
841 plates at 500,000 cells per cell of a six well plate and 100,000 cells per well of a 24
842 well plate. For one biological replicate 4 wells of a six well plate per pooled per
843 experiment. RNA was put into complex with lyovec (Invivogen, cat # lyec-1) to a
844 final concentration of 10ng/µl, and 100µl (1µg RNA) applied per six well and 25µl
845 (250ng RNA) applied per 24 well. After a twenty-four hour incubation, conditioned
846 media was removed and cells were rinsed in cold PBS before being lysed in 300µl
847 (across 4 wells of a six well plate) using cytokine lysis buffer (1% Igepal CA-630, 20
848 mM Tris-HCl (pH 8.0), 137 mM NaCl, 10% glycerol, 2 mM EDTA, 10 µg/mL
849 Aprotinin, 10 µg/mL Leupeptin, and 10 µg/mL Pepstatin). Cells were lysed for 30
850 mins on ice with gentle pipetting. Proteome Profiler Cytokine Array Panel A (R&D
851 Systems, cat # ARY006) was then used for parallel detection of activated cytokines
852 and chemokines in cytosolic lysates or conditioned media according to
853 manufacturer's instructions. Quantification of dot plots was performed using the
854 Quick Spots software (Ideal Eyes Systems, Inc.).
855
856 **In situ Hybridization**
857 Standard DIG-labelled in situ hybridization was performed using the
858 method described in[75]. Multiplex in situ hybridization was performed using
859 RNAscope (Advanced Cell Diagnostics) (*3*, *4*) (*3*) according to the manufacturer's
860 instructions using a custom designed probe for IAP and standard C3 and Slc1a3
861 probes. Iba1+ cells were identified after RNAscope using an Iba1 antibody
862 (Wako).
863
864 **In utero electroporation**
865 In utero electroporation was performed according to the initial protocol [76]
866 with minor modifications. All surgical procedures were performed in accordance
867 with LaGeSo experimental licenses G0079/11 and G0206/16.

868 **Tissue Processing & Histology**

869 For embryonic tissue, the date of the vaginal plug was counted as
870 embryonic day 0.5 (E0.5). Pregnant females at the desired stage were killed by an
871 i.p. injection of 600 mg pentobarbital per kg body weight and death was
872 confirmed by cervical dislocation. Following a midline incision, uterine horns were
873 excised and placed in a dish containing ice cold PBS, where embryonic brains
874 were isolated using microforceps. Brains were immediately fixed in
875 paraformaldehyde (PFA, 4% in PBS) overnight at 4°C. For animals older than P6,
876 animals were given a lethal i.p. injection of 600 mg pentobarbital per kg body
877 weight and transcardially perfused with PBS (10-20ml, depending on age) until the
878 liver was clear, followed by perfusion with 4% PFA (5-20ml, depending on age).
879 Brains were then isolated and fixed overnight in 4% PFA.

880 For in situ hybridization, all solutions were composed using ddH_2O treated
881 with Diethyl pyrocarbonate (DEPC, Sigma, prepared by shaking 1ml DEPC in 1L
882 ddH_2O at 37°C O/N) and per processed by cryosectioning. For cryosectioning,
883 after fixation brains were dehydrated in sequential concentrations of sucrose (15%,
884 30% in PBS) before being embedded in Optimal cutting temperature compound
885 (OCT, Tissue-Tek) and freezing on dry ice. Tissue blocks were stored at -20°C until
886 16µm sectioning on a cryostat at -20°C, when they were collected on positively
887 charged slides (Superfrost, ThermoFischer) and allowed to dry for 1 hr before
888 being re-frozen for storage at -20°C.

889 For paraffin sectioning, fixed brains were dehydrated by ethanol row (30%
890 EtOH, 50% EtOH, 70% EtOH, 80% EtOH, 90% EtOH, 100% EtOH) followed two
891 changes of Xylol and two changes of paraplast before casting in paraffin in metal
892 embedding molds. For sectioning, a Microtome (Leica) was used and 14µm thick
893 sections were collected in 37°C ddH_2O on positively charged slides (Superfrost,
894 ThermoFischer).

895 Nissl Stains were performed by incubation with cresyl violet. Cresyl violet
896 staining solution was prepared by dissolving 0.1g cresyl violet acetate in 100ml
897 ddH_2O O/N. Following addition of 10 drops (~0.3ml) glacial acetic acid, this
898 cresyl acetate solution was filtered. Nissl stain was performed on rehydrated
899 paraffin sections (Xylol II: 5 mins, Xylol I: 5 mins, 3x5 min 100% Ethanol, 3 min 95%
900 Ethanol). Sections were immediately stained in 0.1% Cresyl violet for 3-10
901 minutes, followed by rinsing in dH_2O to remove excess stain. Sections were then
902 differentiated in 95% ethanol for 2-30 minutes, checking microscopically for
903 optimal staining. Sections were then dehydrated by 2x 5 min 100% ethanol
904 washes and cleared with xylol (2 x 5 mins) before mounting with Entellan (Sigma).
905 Immuno Histochemistry (IHC) was performed primarily on cryosections. For
906 paraffin sections, prior to IHC sections were rehydrated and an antigen retrieval
907 step (Boiling 3 x 5 mins in Antigen Unmasking Solution, Vector Labs) was
908 performed prior to blocking. To perform IHC, slides were washed 2 x 5 minutes in
909 PBS, then blocked and permeabilized in blocking solution (2% BSA, 1% Triton
910 X100 in PBS). All further antibody steps use this same blocking solution as diluent.
911 Primary antibodies were diluted 1:200-500 in blocking solution and incubated on
912 sections at 4°C O/N. The following day, slides were washed 3x10 minutes in PBS
913 and then incubated for two hours at room temperature with the appropriate
914 secondary antibody (Dianova). Sections were then washed 2 x 5 mins and stained
915 with Hoechst/DAPI (1:5000 in PBS) for 5 minutes at room temperature. When
916 using adult sections, lipofuscin autofluorescence was quenched by a 10 min
917 incubation with a solution containing 10mM $CuSO_4$ & 50mM NH_4Cl. Sections were
918 then mounted aqueously using Immu-Mount (Shandon). A full list of antibodies
919 used can be seen in Data S6.
920 For Golgi impregnation, fresh brain samples from WT, HP1$\beta^{fl/fl}$Emx1^{Cre},
921 HP1$\gamma^{fl/fl}$Emx1^{Cre} and HP1$\beta/\gamma^{fl/fl}$Emx1^{Cre} of young (3 months) and aged (13-14
922 months) mice were cut into two hemispheres and impregnated in Golgi-Cox

923 solution for 2 weeks as described in [77]. Sholl analysis [78] was performed blind on
924 CA3 hippocampal neurons by using the concentric circles and cell counter plug-
925 ins available for ImageJ. Intersections were quantified across thirty 10μm spaced
926 concentric circles. The Simple neurite tracer plugin (ImageJ) was used to draw
927 representative neurons.

928 The number of Prox1+ and Ki67+ cells in dentate gyrii were quantified by
929 creating a pipeline in CellProfiler (http://cellprofiler.org). Images were first
930 masked such that only the dentate gyrus was visible, then split into individual files
931 by RGB channel (DAPI- blue, ki-67 – green, Prox1-red). Primary objects were
932 identified for each channel using the following parameters: For nuclei, min-
933 diameter 8, max-diameter 14, threshold correction 1.5, distinguishing by shape.
934 For ki67, min-diameter 5, max-diameter 25, threshold correction 1, distinguishing
935 by intensity. Prox1 primary objects were identified using the same settings as
936 nuclei. Primary objects were then related to nuclei, removing false signal, and
937 count was exported to a csv file. To calculate cells/μm, the area of the dentate
938 gyrus measured was quantified manually in Fiji/ImageJ [79]
939 (https://imagej.nih.gov/ij/).

940 The percentage of area occupied by CD68 inside Iba1+ microglia was
941 quantified by creating a pipeline in CellProfiler and analyzing images in three
942 batches. Images were first corrected for illumination, then aligned, and then Iba1
943 primary objects were identified with min pixel size 4 max 150 using an adaptive
944 Otsu threshold strategy with three classes, identifying the foreground and a 0.1
945 lower threshold bound and an adaptive window size of 65. Second and third
946 batches of CD68 stains required minor adjustments to the lower threshold bound
947 for background correction.

948 **Behavioral Experiments**

949 All behavioural experiments were undertaken in the Animal Outcome Core
950 Facility (AOCF) at the Charité. Behavioral tests were performed within the

951 guidelines granted by the LaGeSo under an extension to the experimental license
952 G0079/11 and G0206/16. Prior to behavioral testing, male HP1FEC mice were
953 implanted with subdermal RFID transponders to ensure accurate identification.
954 Behavioral experiments were performed on both young adults (3 months) and
955 aged adults (13-14 months). Prior to each cohort of behavioral testing, all animals
956 were subjected to a modified **S**mithKline Beecham, **H**arwell, **I**mperial
957 College, **R**oyal London Hospital, **p**henotype **a**ssessment (SHIRPA), which ensured
958 animals did not have any gross deficits in vision, audition, grip strength, pina reflex
959 and normal exploratory locomotion. After SHIRPA assessment, behavioral tests
960 were always carried out at the same time of day, with tests spanning a 1 month
961 period. Tests always occurred in the following order: Open Field Activity, Paired-
962 Pulse inhibition, Context-Cued Fear Conditioning, Barnes Maze, Social Activity
963 Monitor, HomeCageScan, Nest Construction.
964 *Open Field Activity:* Animals were placed in the centre of a square
965 enclosure for 10 minutes while an overhead camera records and movement is
966 tracked using the Biobserve Viewer Software. Activity in the 'center zone' and
967 periphery were binned per minute.
968 *Paired-Pulse Inhibition:* Animals were tested two at a time in a 2-box startle
969 box apparatus (TSE systems), which consisted of black soundproofed plexiglass
970 boxes (49cm x 49cm x 49cm). The floors of internal cases were composed of metal
971 bars connected to pressure sensors, which enabled precise measurement of
972 startle response. Upon program start, animals acclimatized for 5 minutes, followed
973 by a program (randomized by trial) that tested response to startle pulse alone
974 (120dB for 40ms) or response to the pulse that had been preceded by a pre-pulse
975 (one of 69dB, 73dB or 81dB for 20ms).
976 *Context-Cued Fear Conditioning*: Animals were analysed two at a time in
977 two adjacent multi-conditioning boxes from TSE Systems. These were designed to
978 be sound proofed and have a sound probe, a camera, and a context arena with a

979 metal grated floor and walls high enough to contain the animal. Context cued fear
980 learning was tested over 5 phases: Phase 1 (Shock): Animals were allowed to
981 acclimatize in the chamber for 4 minutes (Context), which is followed by a 30
982 second sound (Cue), which is immediately followed by a weak electric shock on
983 the floor of the context arena. Phase 2 (Context 24h): The following day, animals
984 were placed back into the context arena and their freezing response was recorded
985 over 3 minutes. Phase 3 (Cue 24h): two hours following phase 2, a cover was
986 placed over the metal bar floor, animals were habituated for 3 minutes and then
987 the cue sound was played for 3 minutes and freezing response was recorded.
988 Phase 4 (Context 7 Days): Exactly as in phase 2, context was tested 7 days
989 following phase 1. Phase 5 (Cue 7 Days): Two hours following Phase 4, animals
990 were tested for freezing response to the cue, as in phase 3.
991 *Barnes Maze*: The Barnes Maze is a circular platform containing 20 holes
992 around the circumference, one hole contains a submerged nest that serves as an
993 escape from the open environment. Animals were trained on the location of the
994 submerged nest. This involved placing the animal in the centre of the platform
995 while loud static noise is played over four 3-minute trials over 4 training days, in
996 which time the mouse could often find the submerged nest. If the mouse could
997 not find the nest by the end of the 3 minutes, the mouse was shown the nest.
998 Once in the nest the mouse was allowed to stay for 30 seconds to allow for
999 positive reinforcement. Following 4 days of training, the nest is removed and
1000 animals were tested on the 5th day (24h test) where mice were placed in the centre
1001 of the platform and their hole seeking behavior is recorded (time to target hole,
1002 errors before target hole, headpokes per hole) over a 90 second testing period.
1003 Animals were then tested one week later (7day test) in the same manner.
1004 *Social Activity Monitor (SAM):* To measure basic interaction and circadian
1005 activity, animals in their home cages were placed on top of RF sensors that detect
1006 motion. Animal activity was then recorded for 14 days using Phenoscoft control

software. SAM data was binned by hour and following data export, RFIDs were decoded to corresponding animal ids and genotypes.

HomeCageScan (Microbehaviors): Animals were recorded individually over 24hs using CleverSys Software for any changes in sterotyped murine behavior. Prior to recording, background cage registration, night/day and transition calibrations were set according to each cage. For data export, data was binned by minute and by hour.

Nest Construction: Because a pilot experiment revealed that a two day separation of male animals from their homecages resulted in hyper aggression upon their return, nest construction was only tested in the aged timepoint. To test nest construction ability, mice were housed individually and given a square piece of densely woven cotton called a 'nestlet' (Ancare). Animals were allowed to habituate with the nestlet for the first 24 hrs. For the second 24hs a new nestlet was supplied and the following morning what remained of the nestlet was weighed and the complexity of the nest was scored based on the standard rubric: (1) The Nestlet is largely untouched (>90% intact). (2) The Nestlet is partially torn up (50-90% remaining intact). (3) The Nestlet is mostly shredded but often there is no identifiable nest site: < 50% of the Nestlet remains intact but < 90% is within a quarter of the cage floor area, i.e. the cotton is not gathered into a nest but spread around the cage. Note: the material may sometimes be in a broadly defined nest area but the critical definition is that 50-90% has been shredded. (4) An identifiable, but flat nest: > 90% of the Nestlet is torn up, the material is gathered into a nest within a quarter of the cage floor area, but the nest is flat, with walls higher than mouse body height (curled up on its side) on less than 50% of its circumference. (5) A (near) perfect nest: > 90% of the Nestlet is torn up, the nest is a crater, with walls higher than mouse body height on more than 50% of its circumference.

Magnetic Resonance Imaging

1035 MRI was performed at a 7 Tesla rodent scanner (Pharmascan 70/16, Bruker,
1036 Ettlingen, Germany) with a 20 mm diameter transmit/receive volume resonator
1037 (RAPID Biomedical, Rimpar, Germany). For imaging the mouse brain a T2-
1038 weighted 2D turbo spin-echo sequence was used (imaging parameters TR/TE =
1039 5505 ms/36 ms, rare factor 8, 6 averages, 46 axial slices with a slice thickness of
1040 0.350 mm, field of view of 2.56 x 2.56 cm, matrix size 256 x 256; scan time
1041 13m12s). MRI data were registered on the Allen mouse brain atlas (ABA) using an
1042 in-house developed MATLAB toolbox ANTx (latest version available under
1043 https://github.com/ChariteExpMri/antx2). The volumes of each single ABA brain
1044 structure were calculated using the back-transformed atlas which matched the
1045 individual T2-weighted images [80]. For section-wise analysis, the mean isocortex
1046 volume per section per genotype per age was calculated and tested using two-
1047 way ANOVA.

1048 **Site specific 5hmC and 5mC Analysis by qPCR**

1049 Genomic DNA was purified from frozen hippocampi using NucleoSpin
1050 Tissue columns (Macherey-Nagel) according to the manufacturer's instructions.
1051 Purified gDNA was subsequently processed using the EpiMark 5hmC Analysis kit
1052 (NEB, cat# E3317) according to the manufacturer's instructions. CpGs of
1053 enzymatically prepared samples were then profiled using primers designed to
1054 amplify over an area containing a single HpaII/MspI site. Primers used for qPCR:
1055 Nnat: ACCCCTCCTTCTCAACATCC & CGCCGAGGTCTACTGGTCT. For IAPEz:
1056 CTTTGAAGGAGCCGAGGGTG & AAGCCTGTCTAACTGCACCAA. qPCR was
1057 performed using the GoTaq qPCR Master mix (Promega) including the CXR
1058 reference dye on a StepOnePlus Thermocycler (Applied Biosystems).
1059
1060

1061 **HP1cTKO Embryonic Stem Cell line**

ESCs possessing *Cbx1*, *Cbx3*, or *Cbx5* conditional alleles were constructed via gene targeting by flanking exons 2 and 3, exon 3, or exon 3, of each gene with LoxP sequences, respectively (fig. S12). Conditional mice were established from each conditional ESC line. *Cbx1*, *Cbx3*, or *Cbx5* mutant mice were next crossed with mice bearing *CreERT2* alleles, to enable excision of the floxed alleles by addition of 4-OH tamoxifen (4-OHT). Triple conditional mutant mice were obtained via crossing the single, or double conditional mice. Triple conditional ESC lines were made in house from the triple conditional mouse blastocysts. ESCs were cultured in D-MEM (Kohjin-bio, #16003550) with 20% fetal bovine serum (Sigma-Aldrich, #172012), MEM nonessential amino acids (GIBCO, #11140-050), L-glutamine (GIBCO, #25030-081), 2-mercaptoethanol (Sigma-Aldrich, #M1753), and LIF (in-house preparation) on mitomycin C-treated (Sigma-Aldrich, #M4287) primary MEF feeder layers. For conditional KO, 4-OH Tamoxifen (SIGMA, #H7904; (Z)-4-Hydroxytamoxifen, ≥98% Z isomer, dissolved in ethanol) was added to medium to a final concentration of 800 nM and cultured for 6 days. The stock solution was prepared as 2 mM (X2500).

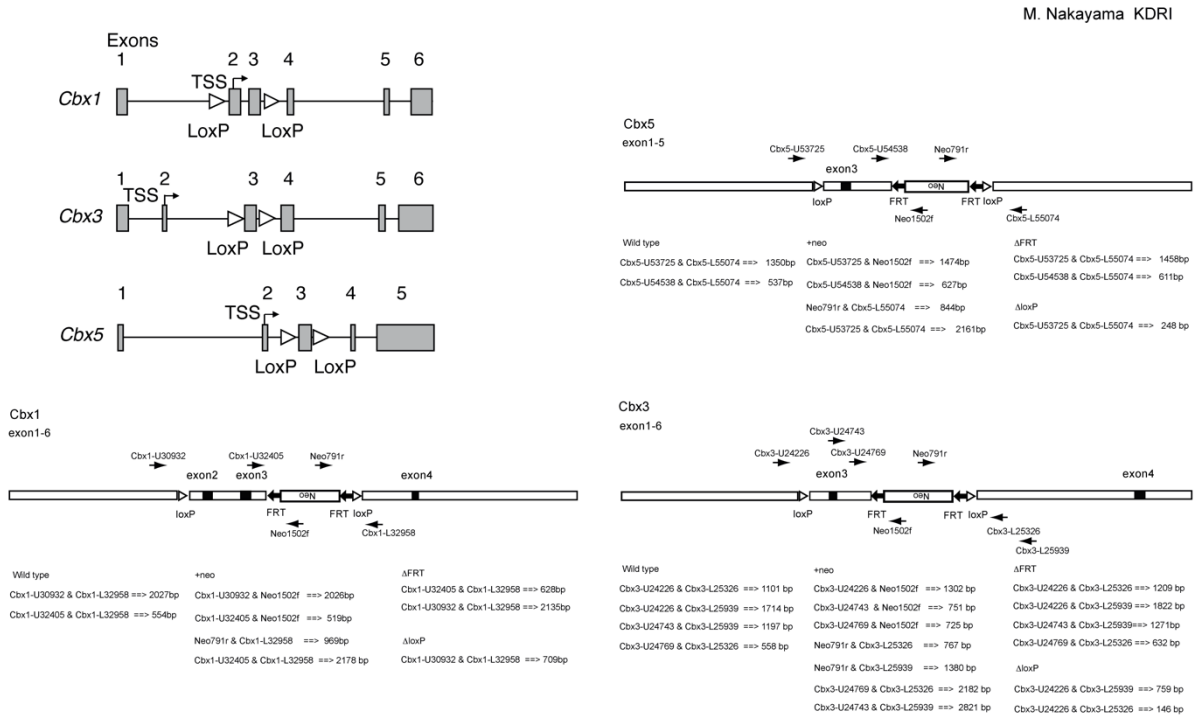

1079 **Extended Data Figure S12.** Targeting of *Cbx1*, *Cbx3*, & *Cbx5* alleles in HP1cTKO
1080 ESCs
1081
1082
1083
1084 **Chromatin Immunoprecipitation (ChIP) & Library Construction**
1085 ChIP experiments and subsequent library preparation, were performed as
1086 previously described [81]. Antibodies used for ChIP can be seen in Data S1.
1087 **Reduced Representation Bisulfite Sequencing (RRBS)**
1088 RRBS was carried out following a previously described method [82] with minor
1089 modifications. 500 ng of genomic DNA was used as a starting material. Bisulfite
1090 conversion was done by the EZ DNA Methylation Gold Kit (Zymo Research,
1091 #D5005) with 50 ng of DNA, per sample. 2x KAPA HiFi Hot Start Uracil+ Ready Mix
1092 (KAPA Biosystems, #KK2801) was utilized for library amplification. PCR
1093 amplification was done for 10 cycles.
1094 **5mC & 5hmC Joint profiling from Hippocampal Lysates**
1095 Hippocampi were isolated in ice cold PBS and DNA was using the QIAamp
1096 Fast DNA Tissue Kit (QIAGEN, cat # 51404). Purified DNA was then used to
1097 generate bisulfite converted or oxidative bisulfite converted RRBS libraries using
1098 the Ovation RRBS kit (TECAN, formerly NuGEN, cat # 0553-32). RRBS libraries
1099 were sequenced in a 50bp paired end configuration with an additional 6bp
1100 allotted to the library index on an Illumina Novoseq 6000.
1101 **Bioinformatics & Data Processing**
1102 Bioinformatic pipelines were written using Snakemake
1103 https://snakemake.readthedocs.io/en/stable/ and deployed on the cluster hosted
1104 by the Berlin Institute of Health (BIH). Scripts for analysis are provided at
1105 https://github.com/qoldt/HP1-Deficiency-Neurodegeneration .
1106 For RNAseq data, fastq files were aligned to GRCm38.p5 using STAR [83] with
1107 the following settings to maximize repeat mapping (--outFilterMultimapNmax 100,

1108 --winAchnorMultimapNmax 100, --outSAMstrandField intronMotif). The
1109 TETranscripts [84] package was used to generate a count table using
1110 gencode.vM16.basic.annotation.gtf and the prepared repeat masker file. The
1111 outputted count table was re-annotated using biomaRt [85] and analyzed for
1112 differential expression using edgeR [86]. Hierarchical clustering and heatmap of
1113 significantly changed transcripts determined from testing between all WT and all
1114 HP1DKO (689 genes, adjusted $p < 0.05$, Data S1) was created from a scaled matrix
1115 using heatmap2.

1116 For IAP RNAseq coverage profiles, known IAP coordinates were obtained
1117 from the UCSC table browser in bed format. Deeptools [87] was used to generate
1118 RPKM normalized 50bp bin bigwig files with the option --extendReads from aligned
1119 RNAseq data. Comatrices were computed to scale regions to an internal size of
1120 500bp with before and after region lengths of 1000bp. Read coverage was plotted
1121 over IAP elements for each genotype at each age using RPKM (per bin) = number
1122 of reads per bin / (number of mapped reads (in millions)* bin length (kb)). Chimeric
1123 transcripts were detected using a combination of LIONS [88] and use of a 1000bp
1124 running window filter in Seqmonk. Inflammatory response was profiled by cross
1125 referencing genes differentially expressed in HP1DKO with the interferome
1126 database [89]. Gene set enrichment and leading edge analysis was performed using
1127 GSEA to query raw count data from aged HP1DKO and wildtype against
1128 c2.cp.reactome.v6.2.symbols.gmt using Signal2noise in gene_set mode with
1129 default parameters. GSEA output was imported into cytoscape using the
1130 EnrichmentMap [90] plugin (Jaccard Overlap combined cut-off = 0.375, k constant =
1131 0.5, node cut-off Q = 0.6 and edge cutoff similarity of 0.53). Network node clusters
1132 were coarsely annotated using the AutoAnnotate [91] plugin which was further refined
1133 using Adobe Illustrator.

1134 5mC and 5hmC RRBS data derived from paired bisulfite (BS) and oxidative
1135 bisulfite (oxBS) reactions was analysed as follows: Reads (R1 and R3 in this case)

1136 were trimmed using trim_galore (https://github.com/FelixKrueger/TrimGalore)
1137 with the parameters --paired -a AGATCGGAAGAGC -a2 AAATCAAAAAAAC .
1138 Reads were then further processed using the NuGEN diversity trimming script (
1139 https://github.com/nugentechnologies/NuMetRRBS/blob/master/trimRRBSdiversit
1140 yAdaptCustomers.py) and aligned to the GRCm38 (mm10) Bisulfite Genome using
1141 Bismark with -p 2 -N 1 --multicore 8. Coverage files were generated using
1142 bismark_methylation_extractor with -p --ignore_r2 3. True 5mC was taken directly
1143 from the oxBS data. To infer 5hmC state, oxBS coverage files were subtracted from
1144 BS coverage files outlined in the created 'Extract 5hmC.R' script , where count
1145 $Count_{5hmC} = Count_{BSmethylated} - Count_{oxBSmethylated}$, $\%_{5hmC} = \%_{BSmethylated} -$
1146 $\%_{oxBSmethylated}$, and the number of unmodified cytosines $Count_{No5hmC}$ is calculated
1147 based on the relationship $\%_{5hmC} = \frac{Count_{5hmC}}{Count_{5hmC} + Count_{No5hmC}} * 100\%$, rounded to the
1148 closest integer. In fringe cases where oxBS signal is higher than BS (5hmC is
1149 negative), 5hmC is set to zero and $Count_{No5hmC}$ is set to $Count_{BSunmethylated}$. Coverage
1150 files from 5mC and 5hmC were tested for differential methylation using methylkit [92]
1151 and intersected with genomic annotations obtained from the UCSC table browser.
1152 Odds ratio for each annotation tested was calculated as follows; given $D_{overlaps}$, the
1153 number of Differentially Methylated Regions (DMRs) that overlap with the
1154 annotation, N_{overlaps}, the number of Non-Differentially Methylated Regions (Non-
1155 DMRs) that overlap with the annotation, D, the total number of DMRs and C, the
1156 total number of observed cytosines:

1157 $$Odds\ Ratio = \frac{\frac{D_{overlaps}}{D - D_{overlaps}}}{\frac{N_{overlaps}}{C - D - N_{overlaps}}}$$

1158 The probability P of drawing $D_{overlaps}$ or more by chance, when drawing D DMRs
1159 from a population of C total cytosines, of which $D_{overlaps}$ and N_{overlaps} are successes
1160 (i.e., overlaping with the annotation) was calculated using the hypergeometric
1161 distribution. This calculation was performed with the 'phyper' function in R which

1162 tests the null hypothesis that the observed number of overlaps is as expected by
1163 chance: $P(X \geq D_{overlaps}) = 1 - phyper(D_{overlaps} - 1, D_{overlaps} +$
1164 $N_{overlaps}, C - (D_{overlaps} + N_{overlaps}), D, lower.tail = TRUE)$. Following the
1165 hypergeometric test, p values were adjusted for multiple comparisons using the
1166 Benjamini-Hochberg procedure based on the number of annotations tested per
1167 dataset. Summary plots of methylation were generated using the plotAnnopeak
1168 function of ChIPseeker and Heatmaps of DMRs were generated using
1169 ComplexHeatmap[93].

1170 HP1cTKO RRBS data was quality trimmed using trim galore using the --rrbs
1171 flag and prepared for analysis using Bismark [94] with bowtie1 and arguments -n 1 -l
1172 45. Bismark coverage files from WT and HP1cTKO were analysed using the R
1173 package methylKit [92], where all differentially methylated bases were extracted that
1174 change more than 25% and pass a corrected significance threshold of q = 0.01.
1175 Differentially methylated bases were then annotated using genomation [95] and
1176 prepared bed files (CpGs, LINEs, SINEs, LTRs, Exons) retrieved from the UCSC
1177 table browser. Jitter plots were created using ggplot2. Circos plot was prepared
1178 by using the circlize package [96]. HP1cTKO eAge was calculated by using the
1179 ~18,000 CpGs included in the MouseEpigeneticClock tool (
1180 https://github.com/EpigenomeClock/MouseEpigeneticClock) [97]. In the WT
1181 sample 966 (5.36%) sites were imputed whereas in HP1cTKO 946 (5.25%) sites
1182 were imputed. The original eAge prediction for WT was -0.9 weeks and the
1183 HP1cTKO 0 weeks resulting in a positive difference of 0.9 weeks (6.3 days).

1184 ChIP raw data was quality filtered using Trimmomatic and aligned to
1185 GRCm38.p5 using bowtie. Deeptools was used to generate bigwig files and
1186 generate heatmaps and profiles [87]. RPGC normalized bigwig files were created
1187 per condition by averaging biological replicates using bamCompare with
1188 parameters --normalizeUsing RPGC --effectveGenomeSize 2652783500 --
1189 operation mean --extendReads 125. Comatrices were computed to scale *IAPEz-int*

1190 regions to 1kb in addition to taking 1kb upstream and 1kb downstream. KAP1,
1191 H3K9me3 and H4K20me3 binding profiles were quantified by creating a centre-
1192 point comatrix at ZFP57 peaks overlapping published murine ICRs in deeptools.
1193 For this annotation, published ZFP57 peaks [42] were subset by their overlap with
1194 published murine ICRs.
1195

1196 **Supplementary Text**

1197

1198 **Behavior**

1199 For behavioral experiments, A total of 42 animals (15 WT, 11 HP1βKO, 6
1200 HP1γKO, 10 HP1β/γDKO) completed the aged time point, while 4 died (2 WT, 1
1201 HP1βKO, 1 HP1β/γDKO) between young and aged testing. Box and whisker plots
1202 for behavioral experiments are comprised of median and 25th and 75th percentiles,
1203 where whiskers extend no further than 1.5X the interquartile range. All line charts
1204 plot the mean, with standard error rendered as a ribbon surrounding the line.
1205 Unless stated otherwise, behavioral experiments were analyzed using Two way
1206 ANOVA with Bonferroni correction for multiple comparisons; where Asterisks (*)
1207 denote tests to between genotype within age (* = $p < 0.05$, ** = $p < 0.01$, *** = $p <$
1208 0.001) and hashtags (#) denote tests within genotype between age (# = $p < 0.05$,
1209 ## = $p < 0.01$, ### = $p < 0.001$).
1210

1211 **HP1cTKO Cell line**

1212 After 7 days of tamoxifen (4-OHT) induced deletion of HP1 proteins in the
1213 HP1cTKO cell line, the cells failed to thrive and cell division became extremely
1214 slow. We suspect that changes to 5hmC and 5mC in HP1cTKO ESCs at 6 days are
1215 in an intermediate stage, similar to that seen previously in SETDB1 -/- ESCs which
1216 were cultured for 4 days [98].

1217

1218 **RNAseq Longitudinal Analysis**

1219 No Differentially expressed genes could be detected between young
1220 HP1γKO and aged HP1γKO. Young HP1βKO and aged HP1βKO showed 184
1221 differentially expressed transcripts among which were increases in C4 and C1qa in
1222 aged HP1βKO. A non-negligible batch effect meant direct comparison of young
1223 HP1DKO and aged HP1DKO was not statistically advisable.

1224

1225 **References:**

1226

1227 1. Madabhushi, R. *et al.* Activity-Induced DNA Breaks Govern the Expression of Neuronal
1228 Early-Response Genes. *Cell* **161**, 1592–1605 (2015).
1229 2. Wu, W. *et al.* Neuronal enhancers are hotspots for DNA single-strand break repair.
1230 *Nature* **593**, 440–444 (2021).
1231 3. Stefanatos, R. & Sanz, A. The role of mitochondrial ROS in the aging brain. *FEBS letters*
1232 **592**, 743–758 (2018).
1233 4. Lu, T. *et al.* Gene regulation and DNA damage in the ageing human brain. *Nature* **429**,
1234 883–891 (2004).
1235 5. Koen, J. D. & Rugg, M. D. Neural Dedifferentiation in the Aging Brain. *Trends in*
1236 *Cognitive Sciences* **23**, 547–559 (2019).
1237 6. Zampieri, M. *et al.* Reconfiguration of DNA methylation in aging. *Mechanisms of Ageing*
1238 *and Development* **151**, 60–70 (2015).
1239 7. Horvath, S. DNA methylation age of human tissues and cell types. *Genome Biol.* **14**,
1240 R115 (2013).

1241 8. De Cecco, M. *et al.* Genomes of replicatively senescent cells undergo global epigenetic
1242 changes leading to gene silencing and activation of transposable elements. *Aging Cell* **12**,
1243 247–256 (2013).
1244 9. Zhang, W. *et al.* A Werner syndrome stem cell model unveils heterochromatin alterations
1245 as a driver of human aging. *Science* **348**, 1160–1163 (2015).
1246 10. De Cecco, M. *et al.* Transposable elements become active and mobile in the genomes of
1247 aging mammalian somatic tissues. *Aging (Albany NY)* **5**, 867 (2013).
1248 11. Shumaker, D. K. *et al.* Mutant nuclear lamin A leads to progressive alterations of
1249 epigenetic control in premature aging. *Proceedings of the National Academy of Sciences*
1250 **103**, 8703–8708 (2006).
1251 12. Ryu, S. H., Kang, K., Yoo, T., Joe, C. O. & Chung, J. H. Transcriptional repression of
1252 repeat-derived transcripts correlates with histone hypoacetylation at repetitive DNA
1253 elements in aged mice brain. *Experimental Gerontology* **46**, 811–818 (2011).
1254 13. Nellåker, C. *et al.* Transactivation of elements in the human endogenous retrovirus W
1255 family by viral infection. *Retrovirology* **3**, 1 (2006).
1256 14. Li, F. *et al.* Transcriptional derepression of the ERVWE1 locus following influenza A
1257 virus infection. *Journal of virology* **88**, 4328–4337 (2014).
1258 15. Lemaître, C., Tsang, J., Bireau, C., Heidmann, T. & Dewannieux, M. A human
1259 endogenous retrovirus-derived gene that can contribute to oncogenesis by activating the
1260 ERK pathway and inducing migration and invasion. *PLOS Pathogens* **13**, e1006451
1261 (2017).
1262 16. Prudencio, M. *et al.* Repetitive element transcripts are elevated in the brain of C9orf72
1263 ALS/FTLD patients. *Hum. Mol. Genet.* **26**, 3421–3431 (2017).
1264 17. Dembny, P. *et al.* Human endogenous retrovirus HERV-K(HML-2) RNA causes
1265 neurodegeneration through Toll-like receptors. *JCI Insight* **5**, (2020).

1266 18. van Horssen, J., van der Pol, S., Nijland, P., Amor, S. & Perron, H. Human endogenous
1267 retrovirus W in brain lesions: Rationale for targeted therapy in multiple sclerosis.
1268 *Multiple Sclerosis and Related Disorders* **8**, 11–18 (2016).
1269 19. Li, W. *et al.* Human endogenous retrovirus-K contributes to motor neuron disease.
1270 *Science translational medicine* **7**, 307ra153-307ra153 (2015).
1271 20. Douville, R., Liu, J., Rothstein, J. & Nath, A. Identification of active loci of a human
1272 endogenous retrovirus in neurons of patients with amyotrophic lateral sclerosis. *Annals of*
1273 *neurology* **69**, 141–151 (2011).
1274 21. Frost, B., Hemberg, M., Lewis, J. & Feany, M. B. Tau promotes neurodegeneration
1275 through global chromatin relaxation. *Nature Neuroscience* **17**, 357–366 (2014).
1276 22. Chang, Y.-H. & Dubnau, J. Endogenous retroviruses and TDP-43 proteinopathy form a
1277 sustaining feedback driving intercellular spread of Drosophila neurodegeneration. *Nat*
1278 *Commun* **14**, 966 (2023).
1279 23. Desplats, P. *et al.* α-Synuclein Sequesters Dnmt1 from the Nucleus: A NOVEL
1280 MECHANISM FOR EPIGENETIC ALTERATIONS IN LEWY BODY DISEASES.
1281 *Journal of Biological Chemistry* **286**, 9031–9037 (2011).
1282 24. Chen, V. *et al.* The mechanistic role of alpha-synuclein in the nucleus: Impaired nuclear
1283 function caused by familial Parkinson's disease SNCA mutations. *Human Molecular*
1284 *Genetics* **29**, 3107–3121 (2020).
1285 25. Geis, F. K. & Goff, S. P. Silencing and Transcriptional Regulation of Endogenous
1286 Retroviruses: An Overview. *Viruses* **12**, 884 (2020).
1287 26. Fukuda, K. & Shinkai, Y. SETDB1-Mediated Silencing of Retroelements. *Viruses* **12**,
1288 596 (2020).
1289 27. Bannister, A. J. *et al.* Selective recognition of methylated lysine 9 on histone H3 by the
1290 HP1 chromo domain. *Nature* **410**, 120–124 (2001).

1291 28. Nielsen, P. R. *et al.* Structure of the HP1 chromodomain bound to histone H3 methylated
1292 at lysine 9. *Nature* **416**, 103 (2002).
1293 29. Singh, P. B. & Newman, A. G. On the relations of phase separation and Hi-C maps to
1294 epigenetics. *R. Soc. open sci.* **7**, 191976 (2020).
1295 30. Stephan, A. H. *et al.* A Dramatic Increase of C1q Protein in the CNS during Normal
1296 Aging. *J Neurosci* **33**, 13460–13474 (2013).
1297 31. Reichwald, J., Danner, S., Wiederhold, K.-H. & Staufenbiel, M. Expression of
1298 complement system components during aging and amyloid deposition in APP transgenic
1299 mice. *Journal of Neuroinflammation* **6**, 35 (2009).
1300 32. Aucott, R. *et al.* HP1-β is required for development of the cerebral neocortex and
1301 neuromuscular junctions. *The Journal of cell biology* **183**, 597–606 (2008).
1302 33. Maksakova, I. *et al.* Distinct roles of KAP1, HP1 and G9a/GLP in silencing of the two-
1303 cell-specific retrotransposon MERVL in mouse ES cells. *Epigenetics & Chromatin* **6**, 1–
1304 16 (2013).
1305 34. Schotta, G. A silencing pathway to induce H3-K9 and H4-K20 trimethylation at
1306 constitutive heterochromatin. *Genes & Development* **18**, 1251–1262 (2004).
1307 35. Takada, Y. *et al.* HP1γ links histone methylation marks to meiotic synapsis in mice.
1308 *Development* **138**, 4207–4217 (2011).
1309 36. Kiefer, L. *et al.* WAPL functions as a rheostat of Protocadherin isoform diversity that
1310 controls neural wiring. *Science* **380**, eadf8440 (2023).
1311 37. Jin, J. *et al.* CTCF barrier breaking by ZFP661 promotes protocadherin diversity in
1312 mammalian brains. 2023.05.08.539838 Preprint at
1313 https://doi.org/10.1101/2023.05.08.539838 (2023).
1314 38. Lv, X. *et al.* Patterned cPCDH expression regulates the fine organization of the
1315 neocortex. *Nature* **612**, 503–511 (2022).

1316 39. Souza, P. P. *et al.* The histone methyltransferase SUV420H2 and Heterochromatin
1317 Proteins HP1 interact but show different dynamic behaviours. *BMC Cell Biology* **10**, 41
1318 (2009).
1319 40. Jiang, Y. *et al.* The methyltransferase SETDB1 regulates a large neuron-specific
1320 topological chromatin domain. *Nature Genetics* **49**, 1239–1250 (2017).
1321 41. Zhao, Y.-T. *et al.* Long genes linked to autism spectrum disorders harbor broad enhancer-
1322 like chromatin domains. *Genome Res.* **28**, 933–942 (2018).
1323 42. Riso, V. *et al.* ZFP57 maintains the parent-of-origin-specific expression of the imprinted
1324 genes and differentially affects non-imprinted targets in mouse embryonic stem cells.
1325 *Nucleic Acids Research* **44**, 8165–8178 (2016).
1326 43. Wu, X. & Zhang, Y. TET-mediated active DNA demethylation: mechanism, function and
1327 beyond. *Nat Rev Genet* **18**, 517–534 (2017).
1328 44. Stevens, B. *et al.* The Classical Complement Cascade Mediates CNS Synapse
1329 Elimination. *Cell* **131**, 1164–1178 (2007).
1330 45. Wu, T. *et al.* Complement C3 Is Activated in Human AD Brain and Is Required for
1331 Neurodegeneration in Mouse Models of Amyloidosis and Tauopathy. *Cell Reports* **28**,
1332 2111-2123.e6 (2019).
1333 46. Hahn, O. *et al.* Atlas of the aging mouse brain reveals white matter as vulnerable foci.
1334 *Cell* **186**, 4117-4133.e22 (2023).
1335 47. Jönsson, M. E. *et al.* Activation of endogenous retroviruses during brain development
1336 causes an inflammatory response. *The EMBO Journal* **40**, e106423 (2021).
1337 48. Karikó, K., Buckstein, M., Ni, H. & Weissman, D. Suppression of RNA Recognition by
1338 Toll-like Receptors: The Impact of Nucleoside Modification and the Evolutionary Origin
1339 of RNA. *Immunity* **23**, 165–175 (2005).

1340 49. Cañadas, I. *et al.* Tumor innate immunity primed by specific interferon-stimulated
1341 endogenous retroviruses. *Nat Med* **24**, 1143–1150 (2018).
1342 50. Smallwood, A., Esteve, P.-O., Pradhan, S. & Carey, M. Functional cooperation between
1343 HP1 and DNMT1 mediates gene silencing. *Genes & Development* **21**, 1169–1178 (2007).
1344 51. Noguchi, H. *et al.* DNA Methyltransferase 1 Is Indispensable for Development of the
1345 Hippocampal Dentate Gyrus. *The Journal of Neuroscience* **36**, 6050–6068 (2016).
1346 52. Hutnick, L. K. *et al.* DNA hypomethylation restricted to the murine forebrain induces
1347 cortical degeneration and impairs postnatal neuronal maturation. *Human Molecular*
1348 *Genetics* **18**, 2875–2888 (2009).
1349 53. Martos, S. N. *et al.* Two approaches reveal a new paradigm of 'switchable or genetics-
1350 influenced allele-specific DNA methylation' with potential in human disease. *Cell Discov*
1351 **3**, 17038 (2017).
1352 54. Barbot, W., Dupressoir, A., Lazar, V. & Heidmann, T. Epigenetic regulation of an IAP
1353 retrotransposon in the aging mouse: progressive demethylation and de-silencing of the
1354 element by its repetitive induction. *Nucleic Acids Res* **30**, 2365–2373 (2002).
1355 55. Sanchez, D. *et al.* Aging without Apolipoprotein D: Molecular and cellular modifications
1356 in the hippocampus and cortex. *Experimental Gerontology* **67**, 19–47 (2015).
1357 56. Stilling, R. M. *et al.* De-regulation of gene expression and alternative splicing affects
1358 distinct cellular pathways in the aging hippocampus. *Front. Cell. Neurosci.* **8**, (2014).
1359 57. de Magalhães, J. P., Curado, J. & Church, G. M. Meta-analysis of age-related gene
1360 expression profiles identifies common signatures of aging. *Bioinformatics* **25**, 875–881
1361 (2009).
1362 58. Hong, S. *et al.* Complement and microglia mediate early synapse loss in Alzheimer
1363 mouse models. *Science* **352**, 712–716 (2016).

1364 59. Liddelow, S. A. *et al.* Neurotoxic reactive astrocytes are induced by activated microglia.
1365 *Nature* **541**, 481–487 (2017).
1366 60. Perez-Nievas, B. G. & Serrano-Pozo, A. Deciphering the Astrocyte Reaction in
1367 Alzheimer's Disease. *Front. Aging Neurosci.* **10**, (2018).
1368 61. Pastuzyn, E. D. *et al.* The Neuronal Gene Arc Encodes a Repurposed Retrotransposon
1369 Gag Protein that Mediates Intercellular RNA Transfer. *Cell* **172**, 275-288.e18 (2018).
1370 62. Holm, M. M., Kaiser, J. & Schwab, M. E. Extracellular Vesicles: Multimodal Envoys in
1371 Neural Maintenance and Repair. *Trends in Neurosciences* **41**, 360–372 (2018).
1372 63. Cocozza, F. *et al.* Extracellular vesicles and co-isolated endogenous retroviruses from
1373 murine cancer cells differentially affect dendritic cells. *The EMBO Journal* **42**, e113590
1374 (2023).
1375 64. Smith, H. L. *et al.* Astrocyte Unfolded Protein Response Induces a Specific Reactivity
1376 State that Causes Non-Cell-Autonomous Neuronal Degeneration. *Neuron* **105**, 855-
1377 866.e5 (2020).
1378 65. Bach, E. A. *et al.* Ligand-Induced Autoregulation of IFN-γ Receptor β Chain Expression
1379 in T Helper Cell Subsets. *Science* **270**, 1215–1218 (1995).
1380 66. Hashioka, S., Klegeris, A., Schwab, C. & McGeer, P. L. Interferon-γ-dependent cytotoxic
1381 activation of human astrocytes and astrocytoma cells. *Neurobiology of Aging* **30**, 1924–
1382 1935 (2009).
1383 67. Mitchell, T. J. *et al.* IFN-gamma up-regulates expression of the complement components
1384 C3 and C4 by stabilization of mRNA. *J. Immunol.* **156**, 4429–4434 (1996).
1385 68. Chakrabarty, P. *et al.* IFN-γ Promotes Complement Expression and Attenuates Amyloid
1386 Plaque Deposition in Amyloid β Precursor Protein Transgenic Mice. *The Journal of*
1387 *Immunology* **184**, 5333–5343 (2010).

1388 69. Li, A. *et al.* IFN-γ promotes τ phosphorylation without affecting mature tangles. *The*
1389 *FASEB Journal* **29**, 4384–4398 (2015).
1390 70. Costa-Mattioli, M. & Walter, P. The integrated stress response: From mechanism to
1391 disease. *Science* **368**, (2020).
1392 71. Zhang, J. *et al.* Neurotoxic microglia promote TDP-43 proteinopathy in progranulin
1393 deficiency. *Nature* **588**, 459–465 (2020).
1394 72. Labzin, L. I., Heneka, M. T. & Latz, E. Innate Immunity and Neurodegeneration. *Annual*
1395 *Review of Medicine* **69**, 437–449 (2018).
1396 73. Wyss-Coray, T. Ageing, neurodegeneration and brain rejuvenation. *Nature* **539**, 180–186
1397 (2016).
1398 74. Horie, K. *et al.* Retrotransposons Influence the Mouse Transcriptome: Implication for the
1399 Divergence of Genetic Traits. *Genetics* **176**, 815–827 (2006).
1400 75. Bormuth, I. *et al.* Neuronal Basic Helix-Loop-Helix Proteins Neurod2/6 Regulate
1401 Cortical Commissure Formation before Midline Interactions. *Journal of Neuroscience* **33**,
1402 641–651 (2013).
1403 76. Saito, T. In vivo electroporation in the embryonic mouse central nervous system. *Nature*
1404 *Protocols* **1**, 1552 (2006).
1405 77. Zaqout, S. & Kaindl, A. M. Golgi-Cox Staining Step by Step. *Front. Neuroanat.* **10**,
1406 (2016).
1407 78. Sholl, D. A. Dendritic organization in the neurons of the visual and motor cortices of the
1408 cat. *J Anat* **87**, 387-406.1 (1953).
1409 79. Schindelin, J. *et al.* Fiji: an open-source platform for biological-image analysis. *Nature*
1410 *Methods* **9**, 676–682 (2012).

1411 80. Koch, S. *et al.* Atlas registration for edema-corrected MRI lesion volume in mouse stroke
1412 models: *Journal of Cerebral Blood Flow & Metabolism* (2017)
1413 doi:10.1177/0271678X17726635.
1414 81. Sharif, J. *et al.* Activation of Endogenous Retroviruses in Dnmt1−/− ESCs Involves
1415 Disruption of SETDB1-Mediated Repression by NP95 Binding to Hemimethylated DNA.
1416 *Cell Stem Cell* (2016) doi:10.1016/j.stem.2016.03.013.
1417 82. Boyle, P. *et al.* Gel-free multiplexed reduced representation bisulfite sequencing for
1418 large-scale DNA methylation profiling. *Genome Biology* **13**, R92 (2012).
1419 83. Dobin, A. *et al.* STAR: ultrafast universal RNA-seq aligner. *Bioinformatics* **29**, 15–21
1420 (2013).
1421 84. Jin, Y., Tam, O. H., Paniagua, E. & Hammell, M. TEtranscripts: a package for including
1422 transposable elements in differential expression analysis of RNA-seq datasets.
1423 *Bioinformatics* **31**, 3593–3599 (2015).
1424 85. Durinck, S., Spellman, P. T., Birney, E. & Huber, W. Mapping Identifiers for the
1425 Integration of Genomic Datasets with the R/Bioconductor package biomaRt. *Nat Protoc*
1426 **4**, 1184–1191 (2009).
1427 86. Robinson, M. D., McCarthy, D. J. & Smyth, G. K. edgeR: a Bioconductor package for
1428 differential expression analysis of digital gene expression data. *Bioinformatics* **26**, 139–
1429 140 (2010).
1430 87. Ramírez, F. *et al.* deepTools2: a next generation web server for deep-sequencing data
1431 analysis. *Nucleic Acids Research* **44**, W160–W165 (2016).
1432 88. Babaian, A. *et al.* LIONS: analysis suite for detecting and quantifying transposable
1433 element initiated transcription from RNA-seq. *Bioinformatics* **35**, 3839–3841 (2019).
1434 89. Rusinova, I. *et al.* Interferome v2.0: an updated database of annotated interferon-
1435 regulated genes. *Nucleic Acids Res.* **41**, D1040-1046 (2013).

1436 90. Merico, D., Isserlin, R., Stueker, O., Emili, A. & Bader, G. D. Enrichment Map: A
1437 Network-Based Method for Gene-Set Enrichment Visualization and Interpretation. *PLOS*
1438 *ONE* **5**, e13984 (2010).
1439 91. Kucera, M., Isserlin, R., Arkhangorodsky, A. & Bader, G. D. AutoAnnotate: A Cytoscape
1440 app for summarizing networks with semantic annotations. *F1000Res* **5**, 1717 (2016).
1441 92. Akalin, A. *et al.* methylKit: a comprehensive R package for the analysis of genome-wide
1442 DNA methylation profiles. *Genome Biol.* **13**, R87 (2012).
1443 93. Gu, Z., Eils, R. & Schlesner, M. Complex heatmaps reveal patterns and correlations in
1444 multidimensional genomic data. *Bioinformatics* **32**, 2847–2849 (2016).
1445 94. Krueger, F. & Andrews, S. R. Bismark: a flexible aligner and methylation caller for
1446 Bisulfite-Seq applications. *Bioinformatics* **27**, 1571–1572 (2011).
1447 95. Akalin, A., Franke, V., Vlahoviček, K., Mason, C. E. & Schübeler, D. genomation: a
1448 toolkit to summarize, annotate and visualize genomic intervals. *Bioinformatics* **31**, 1127–
1449 1129 (2015).
1450 96. Gu, Z., Gu, L., Eils, R., Schlesner, M. & Brors, B. circlize implements and enhances
1451 circular visualization in R. *Bioinformatics* **30**, 2811–2812 (2014).
1452 97. Stubbs, T. M. *et al.* Multi-tissue DNA methylation age predictor in mouse. *Genome*
1453 *Biology* **18**, 68 (2017).
1454 98. Leung, D. *et al.* Regulation of DNA methylation turnover at LTR retrotransposons and
1455 imprinted loci by the histone methyltransferase Setdb1. *PNAS* **111**, 6690–6695 (2014).
1456